Three-dimensional inversion of self-potential data used to constrain the pattern of groundwater flow in geothermal fields

Abderrahim Jardani, A. Revil, A. Boleve, Jean-Paul Dupont

Three-dimensional inversion of self-potential data used to constrain the pattern of groundwater flow in geothermal fields

A. Jardani,[1,2] A. Revil,[1,3] A. Bolève,[3,4] and J. P. Dupont[5]

Received 30 July 2007; revised 24 May 2008; accepted 19 June 2008; published 9 September 2008.

[1] We propose an algorithm to invert self-potential signals measured at the ground surface of the Earth to localize hydromechanical disturbances or to the pattern of groundwater flow in geothermal systems. The self-potential signals result from the divergence of the streaming current density. Groundwater flow can be either driven by topography of the water table, free convection, or deformation of the medium. The algorithm includes the electrical resistivity distribution of the medium obtained independently by DC resistance tomography or electromagnetic methods or by coding the assumed geology in terms of distribution of the electrical resistivity accounting for the effect of the temperature and salinity distributions and possibly constraints from borehole measurements. Inversion of the distribution of the source current density from ground surface and borehole self-potential measurements is achieved by solving the inverse problem using Tikhonov regularization solutions that are compatible with the physics of the primary flow problem. By introducing assumptions regarding the smoothness or the compactness of the source and the three-dimensional distribution of the electrical resistivity of the system, the inverse problem can be solved in obtaining the three-dimensional distribution of the current source density in the ground. However, an annihilator can be added to the inverted source geometry without affecting the measured self-potential field. Annihilators can be obtained from boundary conditions. Synthetic models and a sandbox experiment are discussed to demonstrate the validity of the algorithm. An application is presented to the geothermal field of Cerro Prieto, Baja California, Mexico, using literature data. Inversion of the self-potential and resistivity data allows observing a plume of hot groundwater rising to the ground surface in the central part of the investigated area and discharging to the ground surface in the southwest part. The temperature anomaly associated with the existence of this plume is independently observed by interpolating borehole temperature measurements. We found a good agreement between the distribution of the temperature and the inverted source current density. The proposed method appears therefore as a noninvasive method for remote detection and three-dimensional mapping of subsurface groundwater flow.

Citation: Jardani, A., A. Revil, A. Bolève, and J. P. Dupont (2008), Three-dimensional inversion of self-potential data used to constrain the pattern of groundwater flow in geothermal fields, *J. Geophys. Res.*, *113*, B09204, doi:10.1029/2007JB005302.

1. Introduction

[2] Most of the methods classically used by geophysicists (e.g., seismic, georadar, and electromagnetic methods) are sensitive to the architecture of a geological system or to the saturation of the various fluid phases that are present in porous or fractured media. However, in order to investigate the geometry of groundwater flow in real time, geophysical methods that are directly sensitive to the flow of the groundwater (or CO_2 for CO_2 sequestration problems) are required. Geophysical methods that are directly sensitive to groundwater flow include temperature and the self-potential measurements.

[3] The self-potential method is one of the oldest of all the geophysical techniques. It consists of monitoring or mapping passively the electrical field existing at the ground surface of the Earth. Anthropic signals include for example the 50/60 Hz electrical power interference, metallic pipes in the ground, and moving electrical trains. Once anthropic and telluric signals have been removed, the self-potential signals provide evidence of polarization mechanisms existing in the ground. Any gradient of the generalized electrochemical potentials of charge carriers can generate a source

[1]Department of Geophysics, Colorado School of Mines, Golden, Colorado, USA.
[2]Bureau d'Etudes Alise Environnement, Saint Jacques-sur-Darnétal, France.
[3]INSU-CNRS, LGIT Université de Savoie, Equipe Volcan, Le Bourget-du-Lac, France.
[4]FUGRO, Savoie Technolac, Le Bourget-du-Lac, France.
[5]CNRS-University of Rouen, Morphodynamique Continentale et Côtière, Rouen, France.

0148-0227/08/2007JB005302$09.00

current density. A general formulation of this problem for a multicomponent electrolyte saturating a deformable porous material has been developed recently by *Revil and Linde* [2006], *Revil* [2007], and *Arora et al.* [2007]. The main contributions to the self-potential signals are (1) the streaming potential (related to groundwater flow), (2) the diffusion potential (related to gradients of the chemical potential of ionic species), (3) the thermoelectric effect related to the influence of the temperature upon the chemical potential of charge carriers, and (4) the electro-redox effect associated with ore bodies and contaminant plumes that are rich in organic matter.

[4] In this paper, we are interested only by the streaming potential contribution to self-potential signals and therefore we will assume implicitly that the various contributions of the self-potential signals can be separated (see *Rizzo et al.* [2004] and *Naudet et al.* [2003, 2004] for some examples). The connection between groundwater flow and the self-potential signals can be explained as follows. Groundwater flow generates a driving electrical current density called the streaming current density. Indeed, the surface of minerals that are in contact with water are charged and this fixed charge is counterbalanced by counterions located both in the Stern layer of sorbed counterions and free counterions located in the so-called diffuse layer (the Stern and the diffuse layers form the well-known electrical double layer [*Overbeek*, 1952; *Ishido and Mizutani*, 1981; *Revil and Leroy*, 2001; *Leroy and Revil*, 2004]). The streaming current density is generated by the drag of the excess of electrical charge of the diffuse layer by the flow of the pore water [*Ishido and Mizutani*, 1981]. In the classical formulation of electrokinetic phenomena, the driving or streaming current density is related to the zeta potential, an electrochemical property of the pore water/mineral interface, and the pore fluid pressure field [e.g., *Ishido and Mizutani*, 1981; *Revil et al.*, 2003b]. A recent and alternative formulation relates the driving current density to the excess of electrical charge per unit pore volume times the seepage velocity [see *Revil and Leroy*, 2004; *Revil et al.*, 2005a; *Linde et al.*, 2007; *Bolève et al.*, 2007b]. The divergence of the streaming current density acts as a source term in the Maxwell equations to produce electromagnetic disturbances that can be recorded at the ground surface and in boreholes if their signal-to-noise ratio is strong enough [e.g., *Sill*, 1983].

[5] There are several very promising quantitative investigations reported in the recent literature showing clear self-potential signals associated with groundwater flow in field conditions. For example, *Perrier et al.* [1998] recorded electrical potential variations associated with the variations of the level of two lakes in the French Alps and the resulting groundwater flow and deformation over a period of several years. Once the redox component of the self-potential signals was removed (this component was associated with the presence of graphite in the sedimentary formations), the residual self-potential signals were showing an excellent correlation with the time variation of the difference of altitude of the two lakes. *Kulessa et al.* [2003a, 2003b] showed that self-potential signals are generated during Earth tide deformation of glaciers and groundwater flow in permeable channels organized between the glaciers and the underlying substratum. In geohydrology, *Rizzo et al.* [2004] and *Titov et al.* [2005b] have studied electrical signals associated with the recovery phase of pumping tests performed in an unconfined aquifer [see also *Bogoslovsky and Ogilvy*, 1973]. These self-potential signals were used to determine the distribution of the hydraulic transmissivity of the aquifer by *Straface et al.* [2007]. *Wishart et al.* [2006] used self-potential signals to determine the anisotropy of transmissive fractures in a fractured aquifer. *Jardani et al.* [2006a, 2006b] used the self-potential method to locate sinkholes and crypto-sinkholes in a karstic plateau. *Revil et al.* [2005b] used the self-potential method to locate a paleochannel of a river. *Suski et al.* [2006] validated the physics of streaming potential in the field by monitoring the groundwater flow resulting from the infiltration of water in a ditch. In this experiment, all the material properties arising into the coupled hydro-electric problem were independently measured and used to model successfully the electrical response associated with the infiltration of the groundwater [see also *Revil et al.*, 2002]. This showed that the physics of streaming potential is the same at different scales.

[6] In volcanic areas and geothermal systems, self-potential signals amounting to hundreds of millivolts have been used to determine qualitatively the pattern of groundwater flow [*Zablocki*, 1976; *Corwin et al.*, 1979, 1981; *Ishido*, 1989, 2004; *Revil et al.*, 2001, 2003a; *Aizawa et al.*, 2005; *Aubert and Atangana*, 1996; *Finizola et al.*, 2002, 2003, 2004; *Hase et al.*, 2005; *Bedrosian et al.*, 2007, for some examples]. The same type of analysis can be performed for landslides [*Gex*, 1993] and dams [*Corwin*, 1985; *Black and Corwin*, 1985; *Rozycki et al.*, 2006].

[7] In addition to the investigations reported above, there were also very interesting works reporting the occurrence of self-potential signals associated with shearing and hydrofracturing of water infiltrated media [see *Yoshida*, 2001; *Huang*, 2002; *Yoshida and Ogawa*, 2004; *Soloviev and Sweeney*, 2005; *Moore and Glaser*, 2007], rapid fluid pulses in sandbox experiments [*Crespy et al.*, 2008] and field observations associated with earthquakes and their aftershocks [*Corwin et al.*, 1976; *Huang and Liu*, 2006; *Park et al.*, 2007]. This implies that a full formulation of electromagnetic effects associated with groundwater flow and fracturing should encapsulate the rheological behavior of the earth materials (see *Revil et al.* [2003a] and *Revil* [2007] for a complete model for electro-poro-elastic media).

[8] If the self-potential method seems so promising, one may ask why it has not been used more often? The response lies probably in (1) the multiplicity of sources of self-potential signals and (2) the methods of interpretation used in the past. However, we feel that these two criticisms are not justified. Indeed, with the exception of the redox contribution, the main source of the self-potential anomalies is water flow in porous media (the streaming potential). Thermoelectric and diffusion potentials can be considered as minor components [e.g., *Corwin and Hoover*, 1979; *Massenet and Pham*, 1985]. In addition, *Trique et al.* [2002], *Rizzo et al.* [2004], and *Naudet et al.* [2003, 2004] showed several cases where the redox and streaming potential contributions to self-potential signals could be dissociated and separately investigated.

[9] The second problem with the interpretation of self-potential measurements lies in the methods of interpretation used in the past. Most of the classical methods were based on polarized spheres [e.g., *Yungul*, 1950], dipole current

lines [*Paul*, 1965], source and sink pairs [*Hase et al.*, 2005], or other simple geometries [e.g., *Fitterman*, 1984; *Rozycki et al.*, 2006]. Such types of methods were also used to interpret other potential field problems in magnetism and in gravimetry. As quoted by *Sill* [1983], "although these techniques are useful, they provide little information about the nature of the primary sources," i.e., about the geometry of the groundwater flow or fracturing processes in the present case. More recently, inversion algorithms based on minimization techniques have proved to be very useful to invert potential fields with complex geometries. The application of these methods to invert the electrostatic Poisson's equation is very recent in Earth sciences [*Jardani et al.*, 2006b, 2007; *Minsley et al.*, 2007a, 2007b] but very customary in medical imaging, especially in the study of electroencephalographic and magnetoencephalographic signals [see *Spinelli*, 1999; *Pascal-Marquis et al.*, 2002; *Trujillo-Barreto et al.*, 2004, and references therein]. Other families of algorithms were also developed in the last decade based on cross-correlation algorithms [e.g., *Patella*, 1997; *Revil et al.*, 2001]. In addition, one of the main achievements in the self-potential method has been the development of stable nonpolarizing electrodes with small drifts of few mV per year over several years [see *Perrier et al.*, 1998; *Petiau*, 2000]. With these electrodes, the self-potential method can be used as a cost-effective and reliable method for the long-term monitoring of geological systems over periods of several years.

[10] In this paper, we propose a three-dimensional inversion algorithm to retrieve the geometry of groundwater flow from the record of self-potential signals. Additional geological information is required to constrain the geometry of the source responsible of self-potential signals in order to reduce the nonuniqueness of the inverse problem. A model based on flow in a homogeneous system with boundary conditions can be used to setup an a priori current density model. However, in absence of an a priori model, it is also possible to use null a priori information (see discussion below). We can also impose constraints on the solution by imposing no seepage velocity in some subvolumes of the geological system. An application is performed to the geothermal field of Cerro Prieto in Baja California (Mexico).

2. Underlying Physics

2.1. Relation Between Ground Water Flow and Self-Potentials

[11] We consider a water-saturated rock porous volume Ω, isotropic but possibly inhomogeneous. When fluid flows through such a medium, electrical and hydraulic processes are coupled through the following macroscopic constitutive equations operating at the scale of a representative elementary volume of the porous material [e.g., *Overbeek*, 1952; *Ishido and Mizutani*, 1981; *Revil et al.*, 1999a, 1999b]:

$$\mathbf{j} = \sigma\mathbf{E} - L\left(\nabla p - \rho_f \mathbf{g}\right), \tag{1}$$

$$\mathbf{u} = L\mathbf{E} - \frac{k}{\eta_f}\left(\nabla p - \rho_f \mathbf{g}\right), \tag{2}$$

$$C = \left(\frac{\partial \varphi}{\partial p}\right)_{\mathrm{j}=0} = -\frac{L}{\sigma}, \tag{3}$$

where $\mathbf{j}$ is the (total) electrical current density (in A m^{-2}), $\mathbf{u}$ is the volumetric fluid flux (in m s^{-1}) (Darcy velocity), $\mathbf{E} = -\nabla\varphi$ is the electrical field in the quasistatic limit of the Maxwell equations (in V m^{-1}), φ is the electrical potential (in V), p is the pore fluid pressure (in Pa), $\mathbf{g}$ is the gravitational acceleration vector (in m s^{-2}), σ and k are the electrical conductivity (in S m^{-1}) and permeability (in m^2) of the porous medium, respectively, ρ_f and η_f are the mass density (in kg m^{-3}) and the dynamic shear viscosity (in Pa s) of the pore water, respectively, and L is the electrokinetic coupling term (in m^2 V^{-1} s^{-1}) between the Darcy and generalized Ohm's equations (called the streaming current coupling coefficient), C (in V Pa^{-1}) is the streaming potential coupling coefficient.

[12] An alternative formulation to equation (1) was developed recently by *Revil and Leroy* [2004] and *Revil et al.* [2005a],

$$\mathbf{j} = \sigma\mathbf{E} + \overline{Q}_V \mathbf{u}, \tag{4}$$

where $\overline{Q}_V$ is the excess of charge (of the diffuse layer) per unit pore volume of the porous or fractured material (in C m^{-3}). Note that the charge located in the diffuse layer represents only a small fraction of the total countercharge required to balance the deficit of charge of the mineral surface. As demonstrated by *Leroy and Revil* [2004], most of the counterions are located in the Stern layer.

[13] The advantage of this new formulation is discussed extensively in the work of *Bolève et al.* [2007b]. The excess of charge per unit pore volume is well correlated to the permeability for a wide range of materials as shown in Figure 1. Therefore the interpretation of self-potential data does not require additional material properties than permeability and electrical conductivity at pH $\sim$ 7.

[14] When looking closely at equations (1) and (2), it can be shown that the second equation can be safely decoupled from the first equation if the only component of the electrical field is that produced through the electrokinetic coupling [see *Sill*, 1983]. This means that the electro-osmotic contribution to the hydraulic flow can be safely neglected accounting for the order of magnitude of the electrical field generated through the electrokinetic coupling effect, which is smaller than few volts [e.g., *Sill*, 1983; *Revil et al.*, 1999b, their section 3.1]. With this approximation, we recover the classical Darcy law:

$$\mathbf{u} = -\frac{k}{\eta_f}\left(\nabla p - \rho_f \mathbf{g}\right). \tag{5}$$

[15] The Maxwell equations written in the quasistatic limit give:

$$\nabla \times \mathbf{E} = -\mu\frac{\partial \mathbf{H}}{\partial t} \approx 0, \tag{6}$$

$$\nabla \cdot \mathbf{j} = 0. \tag{7}$$

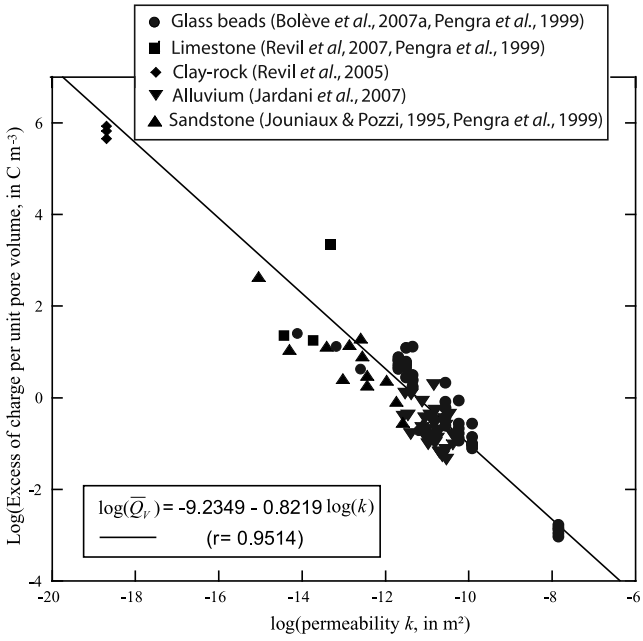

Figure 1. Charge density of the diffuse layer per unit pore volume as a function of the permeability. The experimental data are from different types of rocks. The pH of the solution is between 6 and 9. Experimental data are from *Jouniaux and Pozzi* [1995], *Pengra et al.* [1999], *Revil et al.* [2005a, 2005b], *Bolève et al.* [2007a], *Revil et al.* [2007], and *Jardani et al.* [2007].

[16] The coupling between the electrokinetic equations and finite deformation of a porous body has been investigated recently by several authors, especially in the field of biomechanics [*Frank and Grodzinsky*, 1987; *Levenston et al.*, 1999; *Huygue et al.*, 2004]. We note ρ_f is the density of the pore water and ϕ the porosity ($m_f = \rho_f \phi$ is the mass of the pore water per unit volume of the porous material). The continuity equation for the mass of the pore fluid in a deforming porous medium can be written in term of the volumetric deformation ε of the porous material and time variation of the pore fluid pressure by [*Palciauskas and Domenico*, 1989],

$$\nabla \cdot \left(\rho_f \mathbf{u}\right) = -\rho_f \left[\xi \frac{d\varepsilon}{dt} + \left(\frac{1}{R} - \frac{\xi}{H}\right)\frac{dp}{dt}\right] + \rho_f Q, \tag{8}$$

$$\frac{1}{R} - \frac{\xi}{H} = \frac{1}{\rho_f}\left(\frac{\partial m_f}{\partial p}\right)_{\varepsilon}, \tag{9}$$

$$\frac{1}{H} = \frac{1}{\rho_f}\left(\frac{\partial m_f}{\partial \sigma}\right)_{p}, \tag{10}$$

$$\frac{1}{R} = \frac{1}{\rho_f}\left(\frac{\partial m_f}{\partial p}\right)_{\sigma}, \tag{11}$$

where σ is the mean stress (in Pa) and Q is a volumetric source or sink term for water. The coefficients R, ξ, and H are the Biot coefficients of linear poro-elasticity (R and H are expressed in Pa while ξ is dimensionless). The coefficient $1/R$ represents a measure of the change in water content for a given change in pore fluid pressure when the porous material is permitted to drain freely, $(1/R - \xi/H)$ represents a measure of the amount of water which can be forced into a porous material under pressure while the volume of the material is kept constant, and $1/H$ represents a measure of the change in water content for a given change in confining stress when the material is permitted to drain freely. Despite the fact that these equations were initially derived to model poro-elastic deformation, they can be used to describe irreversible deformation as shown by *Palciauskas and Domenico* [1989].

[17] Combining equations (4) and (7) yields a Poisson equation for the self-potential φ (expressed in V),

$$\nabla \cdot (\sigma \nabla \varphi) = \Im, \tag{12}$$

and where $\Im$ is the volumetric current density (in A m^{-3}). Using equation (8) for a slightly compressible pore fluid, this volumetric current density is given by,

$$\Im = \overline{Q}_V \nabla \cdot \mathbf{u} + \nabla \overline{Q}_V \cdot \mathbf{u}, \tag{13}$$

$$\Im = -\overline{Q}_V \xi \frac{d\varepsilon}{dt} - \overline{Q}_V \left(\frac{1}{R} - \frac{\xi}{H}\right)\frac{dp}{dt} + \overline{Q}_V Q + \nabla \overline{Q}_V \cdot \mathbf{u}, \tag{14}$$

where $\overline{Q}_V$ is defined above. In steady state conditions, equation (14) reduces to,

$$\Im = \overline{Q}_V Q + \nabla \overline{Q}_V \cdot \mathbf{u}. \tag{15}$$

[18] From equation (15), it is obvious that there are some groundwater flow patterns that have no self-potential signatures at the surface of the Earth. By analogy with magnetization and gravity potential field problems [*Parker*, 1977], we call these flow patterns "annihilators." For example, we can assume groundwater flows in a confined homogeneous aquifer of infinite extent. The fluid flow accompanies streaming current with it, but this circulating streaming current is divergenceless if the volumetric charge density is uniform over the entire aquifer. However, if the coupling coefficient is different in subregion A from that in the remaining region (B), the streaming current in region A (or B), the magnitude of which is referred to that in region B (A), brings about self-potential anomaly on the ground surface. This shows clearly that there are limitations to the use of the self-potential method to determine the pattern of groundwater flow that were not addressed in our previous paper [*Jardani et al.*, 2007].

[19] In the study of self-potential signals, an annihilator corresponds to a nonzero distribution of streaming current density (and its associated flow field) that produces no self-potential anomaly for a particular source geometry. An annihilator can be added to its respective source geometry without affecting the measured self-potential field. It follows that a horizontal aquifer with variable current density is indistinguishable from the same aquifer with the same current density plus a uniform source free streaming

current density. Hence an infinite variety of source current densities can be conceived for an infinite aquifer, all producing precisely the same self-potential field. However, if the boundary conditions are known, annihilators can be retrieved.

[20] We show, in the next section, that despite this limitation, inversion of self-potential is a promising approach in getting information about the pattern of groundwater flow, if not in inverting the exact flow field distribution.

2.2. A Two-Step Analysis of the Self-Potential Response

[21] The inversion of the self-potential data recorded at the ground surface of the Earth or in boreholes seeks to retrieve the maximum of information related to the source (its directivity, its localization, and its amplitude). The total current density can be written as,

$$\mathbf{j} = \sigma \mathbf{E} + \mathbf{j}_s, \tag{16}$$

where, from equation (4), $\mathbf{j}_s = \overline{Q}_V \mathbf{u}$ is the (source) streaming current density. Using the Green's method of integration, the electrical potential distribution is written as [*Patella*, 1997],

$$\varphi(P) = \frac{1}{2\pi} \int_{\Omega} \rho(M) \frac{\nabla \cdot \mathbf{j}s(M)}{MP} dV + \frac{1}{2\pi} \int_{\Omega} \frac{\nabla \rho(M)}{\rho(M)} \cdot \frac{\mathbf{E}(M)}{MP} dV, \tag{17}$$

where MP is the distance from the source, located at position $M(\mathbf{r}')$, to the self-potential station located at position $P(\mathbf{r})$ where the self-potential signal is recorded. The first term of the right-hand side of equation (17) corresponds to the primary source term while the second term corresponds to secondary sources associated with heterogeneities in the distribution of the electrical resistivity in the medium. The primary sources can be retrieved only if the resistivity distribution is known and used to evaluate the secondary sources.

[22] It is possible to rewrite equation (17) as the following convolution product [*Spinelli*, 1999; *Trujillo-Barreto et al.*, 2004, their equation (1)],

$$\varphi(P) = \int_{\Omega} \mathbf{K}(P, M) \mathbf{j}_s(M) dV, \tag{18}$$

where $\mathbf{K}(P, M)$, the linear mapping function, is called the kernel by *Trujillo-Barreto et al.* [2004]. The elements of the kernel are the Green functions connecting the self-potential data at a set of measurement stations P located at the ground surface and the sources of current density at a set of source points M located in the conducting ground. The kernel $\mathbf{K}$ depends on the number of measurement stations at the ground surface, the number of discretized elements in which the source current density is determined, and the resistivity distribution. The resistivity distribution can be characterized from a number of geological units, each with a constant resistivity value. A vector of noise can be also be added to the right-hand side of equation (18). In the case of self-potential mapping, the noise can arise because of the unknown heterogeneity of the electrical resistivity close to the location of the electrode. In this case, the measurement of self-potential can be considered as a random process described by a probability distribution that can be sampled by making several self-potential measurements around the same station. In the case of self-potential monitoring with a network of fixed electrodes [see *Rizzo et al.*, 2004], the noise corresponds to anthropic and telluric signals.

[23] The self-potential is measured on a set of N self-potential stations. The current density $\mathbf{j}_S$ is discretized over M elements. Each element of the discretized grid can be characterized by a small volume element. It is either possible to characterize the source by the distribution of the volumetric current density $\Im$ [see *Minsley et al.*, 2007a] or by a vectorial current density (this paper). In our case, the forward problem is related to the determination of the kernel $\mathbf{K}$ in equation (18). The computation of the Green functions entering $\mathbf{K}$ incorporates the resistivity distribution of the model by solving the Poisson equation numerically for $3M$ elementary dipoles using the finite element method (see Appendix A). In our case, the three-dimensional inversion corresponds to the determination of the three components of the current density for each discretized element of the medium (two components for two-dimensional inversion). This is clear that in most case, the inverse problem is strongly underdetermined.

3. Inversion of Self-Potential Data

[24] In the previous section, we have shown that it is possible to compute the electrical potential distribution of a source or a distribution of sources buried in the conductive ground. In this section, we discuss the inverse problem. Using the distribution of the measured potential values at the ground surface, we look for the distribution of the source current density that is responsible for the measured self-potential distribution. This problem is known to be nonunique [see *Pascal-Marquis et al.*, 2002; *Trujillo-Barreto et al.*, 2004; *Minsley et al.*, 2007a]. In other words, an infinite number of source configurations can produced the same measured data. Therefore it is important to add additional constraints or a priori information regarding the number of sources or the spatial extension of the source to reduce the space of the solution. Additional measurements in some boreholes or additional constraints can help to reduce the nonuniqueness of the inverse problem.

3.1. Tomography of Ground Water Flow

[25] The first criterion for inversion requires that the predicted data must fit, or agree with, the observed data. This condition requires the use of a quantitative measure of the agreement between both data sets, known as the data misfit function ψ_d. From equation (18), this function is defined by,

$$\psi_d = \| \mathbf{W}_d(\mathbf{K}\mathbf{m} - \varphi_d) \|_2, \tag{19}$$

where $\|\mathbf{v}\|_2 = (\mathbf{v}^T\mathbf{v})^{1/2}$ denotes the Euclidian (L_2) norm, $\mathbf{K} = (\mathbf{K}_{ij}^x, \mathbf{K}_{ij}^y, \mathbf{K}_{ij}^z)$ is the $N \times 3M$ kernel matrix corresponding to the self-potentials, which can be measured by each component of a sources of coordinates $\mathbf{m} = (\mathbf{J}_i^x, \mathbf{J}_i^y, \mathbf{J}_i^z)$ (N is the number of self-potential stations while M is the disctretized elements composing the ground, $3M$ represents

the number of elementary current sources to consider, two horizontal components and one vertical component), φ_d is vector of N elements corresponding to the self potential data measured at the ground surface and in boreholes, and $\mathbf{W}_d$ = diag $\{1/\varepsilon_1, \ldots, 1/\varepsilon_N\}$ is a square diagonal weighting $N \times N$ matrix. Elements along the diagonal of this matrix are the reciprocal of the standard deviation σ_i squared $\varepsilon_i = \sigma_i^2$. The other components of this matrix are set to zero if the noise on the data is uncorrelated. *Linde et al.* [2007] have shown that the probability distribution of the self-potential measurements in the field corresponds to a Gaussian distribution. As mentioned above, the inversion of self-potential data is ill-posed and does not have a unique solution. This complication arises because there are a finite number of inaccurate data describing the model response and the number of observations is much smaller than the number of unknowns, 3 $M \gg N$ [*Menke*, 1989].

[26] To reduce the number of solutions that equally reproduce the observed data, an additional criterion must be introduced to distinguish the model that most likely represents the subsurface source distribution among the range of possible models. Measuring the structural complexity of a model serves as a good criterion for this purpose. A model objective function ψ_m, is introduced,

$$\psi_m = \| \mathbf{W}_m(\mathbf{m} - \mathbf{m}_0) \|_2, \tag{20}$$

where $\mathbf{W}_m$ is a $3(M-2) \times 3M$ weighting matrix (e.g., the flatness matrix or the differential Laplacian operator), $\mathbf{m}$ is the vector of $3M$ model parameters, and $\mathbf{m}_0$ is a reference model. If we use a null distribution of prior information ($\mathbf{m}_0 = 0$), the inversion algorithm corresponds to a damped weighted linear least squares or biased linear estimation problem.

[27] Using the differential Laplacian operator (second order derivative), the matrix $\mathbf{W}_m$ is given by [*Menke*, 1989],

$$\mathbf{W}_{\mathbf{m}}^2 = \begin{bmatrix} 1 & -2 & 1 & 0 & \cdots & 0 \\ 0 & 1 & -2 & 1 & \cdots & 0 \\ \vdots & & \ddots & \ddots & & \vdots \\ \vdots & & & \ddots & \ddots & \vdots \\ 0 & \cdots & 1 & -2 & 1 & 0 \\ 0 & \cdots & 0 & 1 & -2 & 1 \end{bmatrix}. \tag{21}$$

This operator smoothes the final result of the inversion. The criteria of data misfit and model objective function place different, and competing, requirements on the models. The best model will be one that minimizes the model objective function, ψ_m, while fitting the data within an acceptable range of data misfit, ψ_d. To harness the benefits of both criteria, it is necessary to determine how to control the contribution of each in order to obtain the best solution. The roles of data misfit and model objective function are balanced using Tikhonov regularization [*Tikhonov and Arsenin*, 1977] through a global objective function, ψ, defined as,

$$\psi = \| \mathbf{W}_d(\mathbf{K}\mathbf{m} - \varphi_d) \|_2 + \lambda \| \mathbf{W}_m(\mathbf{m} - \mathbf{m}_0) \|_2, \tag{22}$$

where λ is a regularization parameter under the constraint that $0 < \lambda < \infty$.

[28] The solution of the problem corresponding to the minimum of the cost function ψ is given by [*Hansen*, 1998]:

$$\mathbf{m}^* = \left[\mathbf{K}^T(\mathbf{W}_d^T\mathbf{W}_d)\mathbf{K} + \lambda(\mathbf{W}_m^T\mathbf{W}_m)\right]^{-1} \cdot \left(\mathbf{K}^T(\mathbf{W}_d^T\mathbf{W}_d)\varphi_d + \lambda(\mathbf{W}_m^T\mathbf{W}_m)\mathbf{m}_0\right). \tag{23}$$

[29] An important question regarding the regularized inversion concerns the particular choice of the regularization parameter λ *Haber and Oldenburg* [2000] proposed a generalized cross-validation (GCV) procedure as an efficient tool for selecting the global regularization parameter. Their inverse algorithm proceeds on an iteration by iteration basis, and the optimum regularization weight is modified in each iteration step. Another popular approach is the *L*-curve criterion [*Hansen*, 1998]. The *L*-curve is a plot of the norm of the regularized smoothing solutions ψ_m versus the norm of the data misfit function ψ_d. This dependence exhibits often an *L*-shaped curve, which reflects the heuristics that for large values of the regularization parameter the residual increases without reducing the model norm of the solution much while for small values of the regularization parameter the norm of the solutions increases rapidly without much decrease in the data residual. Thus the best regularization parameter should lie on the corner of the *L*-curve.

[30] As the self-potential sources are mainly dipolar in nature [*Revil et al.*, 2001; *Minsley et al.*, 2007a], the Green function decays as $1/r^2$ if the Earth has a constant resistivity, where r is the distance between the source and the self-potential stations. Therefore because the sensitivity of the self-potential field decays quickly with the distance, the inversion of surface self-potential data, without the use of a depth weighting function, can generate a shallow source current density distribution. The resulting solution in terms of groundwater flow would be not hydrogeologically or hydromecanically meaningful. This is true for example when several aquifers contribute to the self-potential signals (see *Titov et al.* [2005a] for a field example). The use of a depth-weighting function is then necessary to counteract this drawback. To provide cells at depth with equal probability of obtaining nonzero values during inversion, a generalized depth weighting function can be incorporated into the model objective function (see *Li and Oldenburg* [1998] and *Minsley et al.* [2007a] for some details). The depth weighting ($N \times 3M$) matrix is designed to match the overall sensitivity of the data set to a particular cell [e.g., *Spinelli*, 1999],

$$\mathbf{S} = \mathrm{diag}\left(\frac{1}{N}\sqrt{\sum_{j=1}^{N}(K_{ij})^2}\right). \tag{24}$$

The solution of the inverse problem is then given by [*Tikhonov and Arsenin*, 1977],

$$\mathbf{m}_w = \left[\mathbf{K}_\mathbf{w}^T(\mathbf{W}_d^T\mathbf{W}_d)\mathbf{K}_\mathbf{w} + \lambda(\mathbf{W}_m^T\mathbf{W}_m)\right]^{-1} \cdot \left(\mathbf{K}_\mathbf{w}^T(\mathbf{W}_d^T\mathbf{W}_d)\varphi_d + \lambda(\mathbf{W}_m^T\mathbf{W}_m)\mathbf{m}_0\right). \tag{25}$$

where $\mathbf{K}_w = \mathbf{K}\mathbf{S}^{-1}$. The model is then given by $\mathbf{m}^* = \mathbf{S}\mathbf{m}_\mathbf{w}$. This depth weighting is not needed if borehole self-potential data (corrected for the temperature dependence of the

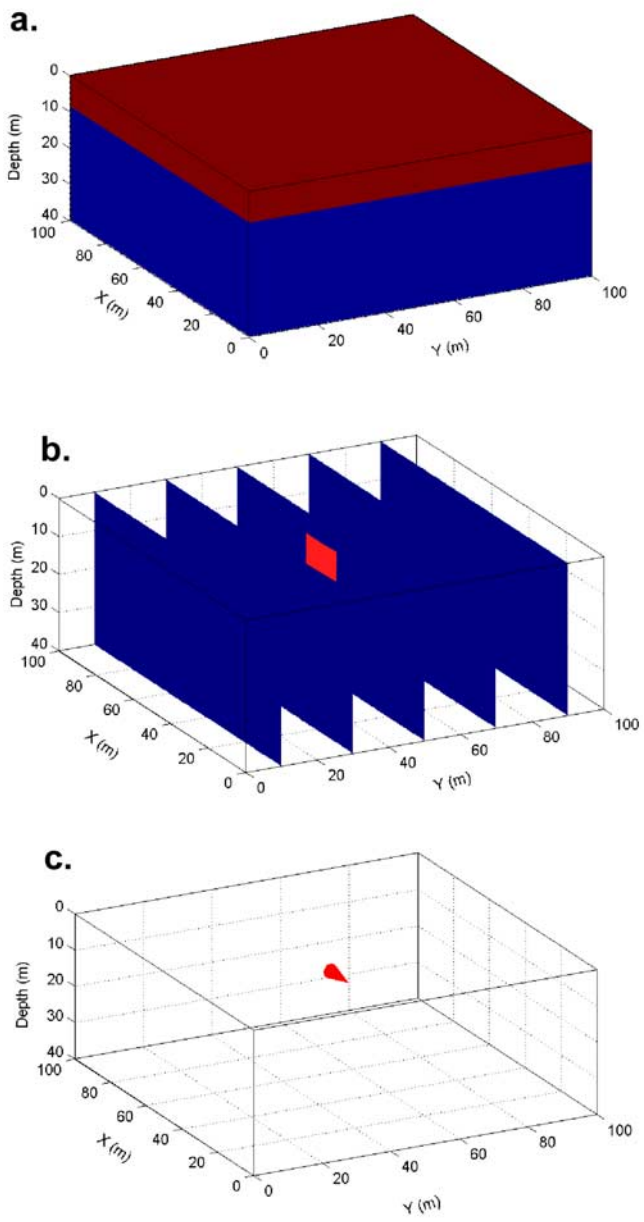

Figure 2. Synthetic model. (a) The synthetic model is composed of two layers. The resistivity of the upper layer is 10 Ω m, and its thickness is 10 m. The second layer has a resistivity of 100 Ω m and a thickness of 30 m. (b) Position of the source. The magnitude of the source current density is 10 mA m^{-2}. (c) Direction of the current source density (see also Figure 4).

electrode potentials, e.g., 0.2 mV/°C for the Petiau electrodes) are available.

[31] Finally, one can also employ a current density positivity constraint when needed. Note also that in our approach, we assume that the resistivity distribution is known. A complete analysis of the uncertainty of the inverted current density distribution associated with the uncertainty of the resistivity model will be investigated in a future work.

3.2. Localization of Compact Self-Potential Sources

[32] Fracturing yields localized electrokinetic sources. In this case, compactness can be used as a criterion to locate more properly the extension of the source. Compactness in the regularization of the inverse problem was used recently by *Minsley et al.* [2007a] to interpret self-potential data associated with pumping tests. *Moore and Glaser* [2007] have shown that hydraulic fracturing produces detectable self-potential signals that are compact in space [see also *Crespy et al.*, 2008]. A compact source can also be obtained if we use a first order differential operator in equation (25),

$$\mathbf{W}_{\mathbf{m}}^{1} = \begin{bmatrix} 1 & -1 & 0 & 0 & \cdots & 0 \\ 0 & 1 & -1 & 0 & \cdots & 0 \\ \vdots & & \ddots & \ddots & & \vdots \\ \vdots & & & \ddots & \ddots & \vdots \\ 0 & \cdots & 0 & 1 & -1 & 0 \\ 0 & \cdots & 0 & 0 & 1 & -1 \end{bmatrix}, \tag{26}$$

rather than the Laplacian operator given by equation (21).

3.3. Synthetic Tests

[33] To test our algorithm, we use the synthetic case shown in Figure 2. The system is composed of two layers. The resistivity of the upper layer is 10 Ohm m and its thickness is 10 m. The second layer has a resistivity of 100 Ohm m and a thickness of 30 m. The source is characterized by a current density of magnitude 10 mA m^{-2}. The polarized volume has the following coordinates: $x \in (50, 60)$ m, $y \in (40, 50)$ m, and $z \in (10, 20)$ m.

[34] The distribution of the self-potential is obtained by solving the Poisson's equation, equation (12), using the finite element commercial code Comsol Multiphysics 3.3. A total of 48 equally spaced stations are used at the top surface of the system to simulate measurement stations for the self-potential signals (Figure 3a). We invert the distribution of the source streaming current density from these discretized synthetic self-potential data (Figure 3). The direction of the source current density is shown in Figures 4a, 4c, and 4e and is downward with two specified angles. We use a null a priori model ($\mathbf{m}_0 = 0$) and the first-order differential operator to regularize the inverse problem because the source is compact. The result of the inversion is shown on Figures 3 and 4. The choice of the regularization parameter is illustrated in Figure 5 by the *L*-shape method.

[35] The result of the inversion is in good agreement with the synthetic model (compare Figures 2c and 3c) both in terms of the intensity of the current density, the direction (Figure 4), and the position of the source. Note that the intensity of the inverted current density (6.3 mA m^{-2}) is only slightly smaller than the true current density (10 mA m^{-2}) showing the accuracy of the proposed method (the use of the smoothness operator yields an inverted current density smaller because the source is spreading over a larger volume).

[36] The robustness of the inverse problem has been tested by adding white noise to the sampled self-potential data. The intensity of the white noise was 10% of the amplitude of the self-potential anomaly (this is typically the level of noise observed in the field data discussed below in section 4). The result of the inversion is shown on Figures 6a

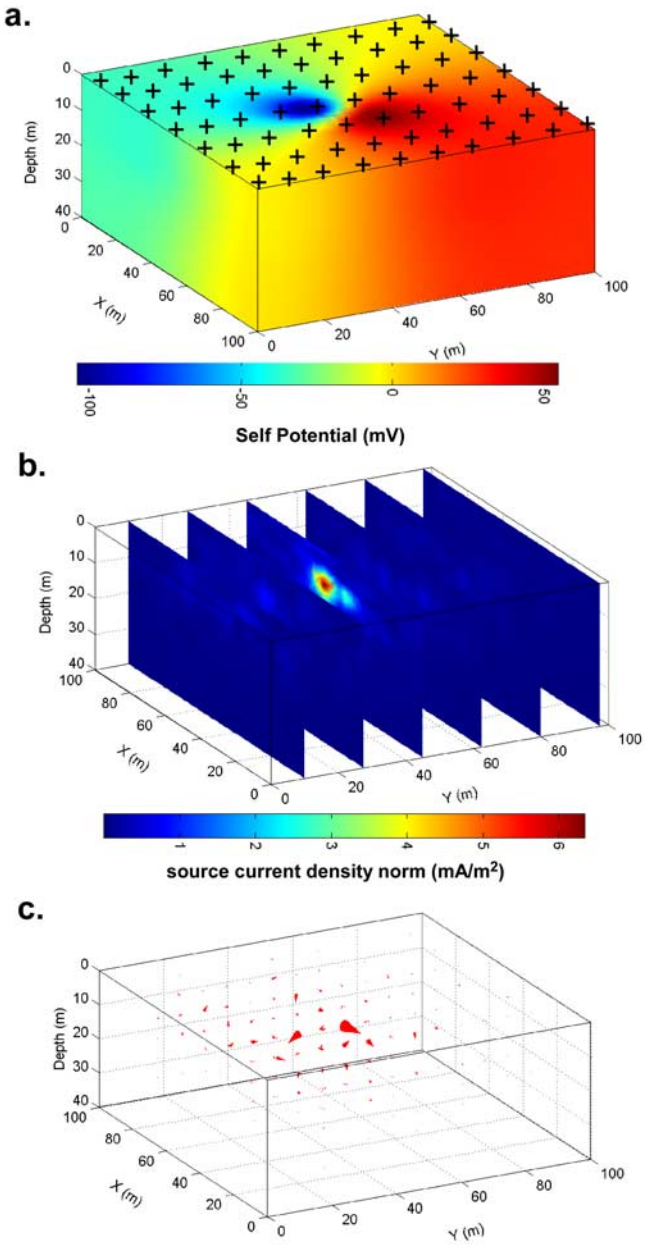

Figure 3. Result of the three-dimensional inversion of the source current density. (a) Distribution of the self-potential over the medium. The self-potential is sampled at the top surface of the system where the crosses are located. (b) Result of the inversion in terms of distribution of the magnitude of the current density (the maximum of the distribution is 6.3 mA m^{-2}). (c) Directions of the inverted source current density using the first derivative operator for the regularization of the inverse problem (no a prior model used).

and 6b. We are able to retrieve correctly the position of the source and its direction. This test demonstrates the robustness of our algorithm. The second test concerns the resistivity distribution. If the resistivity distribution is unknown, one may be attempted to use a homogeneous resistivity distribution. Using the same synthetic model as before, the result of the inversion is shown, in this case, in Figures 6c and 6d. Clearly, the inverted result is grossly wrong both in term of amplitude and direction of the source current density vector. If resistivity tomograms are not available, it is certainly better to code the assumed geology in terms of resistivity distribution than to use a homogeneous Earth model.

3.4. Interpretation of a Pulse Injection in a Sandbox

[37] Synthetic tests like the one discussed above are useful to benchmark the algorithm, but they do not replace a real experiment. Recently, *Crespy et al.* [2008] performed a controlled sandbox experiment that can be used to test the previous algorithm (see Figure 7). In this experiment, ~0.5 mL of water was abruptly injected through a small vertical capillary with its outlet located at a depth of 15 cm (9 cm above the bottom of the tank) in the middle of the sandbox. The self-potential signals resulting from the pulse injection of water were measured using 32 sintered Ag/AgCl electrodes located at the surface of the tank. These electrodes were connected to a voltmeter with a sensitivity of 0.1 μV and an acquisition frequency of 1.024 kHz. The electrodes were all sampled simultaneously. The self-potential anomaly is negative because of the source term $\Im = \nabla\overline{Q}_V \times \mathbf{u}$ in the Poisson equation at the outlet of the capillary ($\overline{Q}_V = 0$ in the capillary and $\overline{Q}_V > 0$ in the sand).

[38] We applied our algorithm to the self-potential anomaly observed at the top surface of the tank when it reached its maximum amplitude (30 ms after the start of the injection). The result is shown in Figure 8. We use the first-order differential operator to regularize the inverse problem because the source is assumed to be compact. The streaming current density associated with the complete spherical radial flow belongs to the "annihilator" described above, so it cannot be inferred by the inversion. No a prior model was used. However, we used the depth dependent normalization given by equation (24) and the positions of the insulating boundary conditions and the reference electrode were used to determine the kernel.

[39] The compact source is located at source point S_p(29 ± 2 cm, 24 ± 2 cm, 10 ± 1 cm). This is consistent with the true position of the outlet of the capillary in the tank S_{true}(29 cm, 24 cm, 9 cm). This illustrates the capability of our approach in locating the causative source of self-potential signals at depth when the support volume of the source is small with respect to the distance between the position of the center of the source and the observation stations. It would be interesting to apply this principle to the shock waves propagating along faults [see *Revil and Cathles*, 2002] and along the conduits of mud volcanoes [*Revil*, 2002].

4. Application to Cerro Prieto

[40] The Cerro Prieto geothermal field is located in the alluvial plain of the Mexicali Valley, northern Baja California, Mexico, at about 35 km southeast of the city of Mexicali (Figure 9). The morphology of the Mexicali Valley is characterized by the presence of the elongated Cucapah range striking predominantly NW–SE and consisting of Upper Cretaceous granite, which has intruded and metamorphized the Cretaceous and/or Paleozoic sediments [*de la Peña and Puente*, 1979]. The only prominent

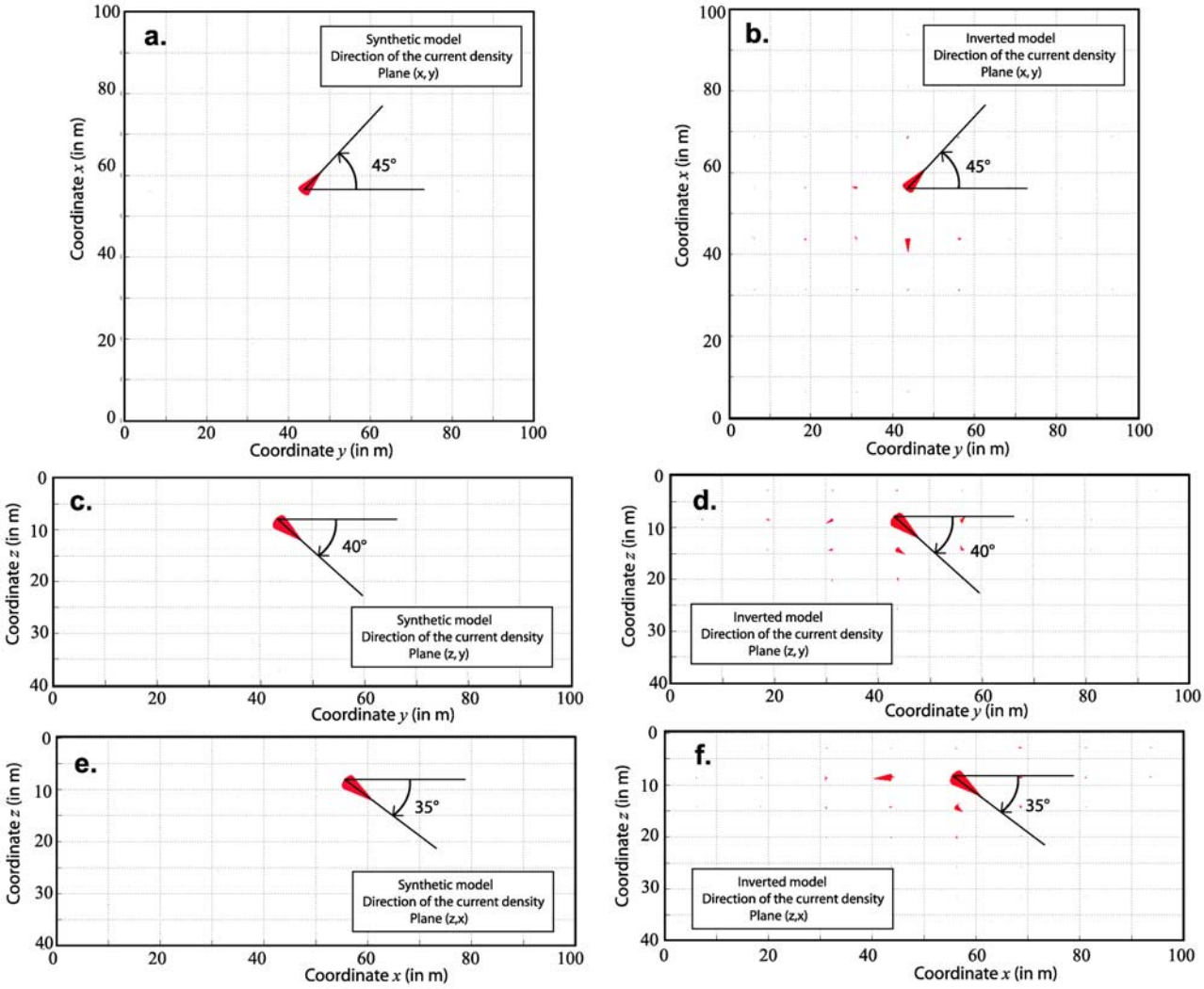

Figure 4. Comparison between the direction of the source current density in the synthetic model and the result of the inversion of the source current density from the self-potential data sampled at the top surface of the system. (a, b) In the plane (x, y), direction of the source current density vector for the synthetic case (left-hand side) and the result of the inversion (right-hand side). (c, d) Same in the plane (z, y). (e, f) Same in the plane (z, x). The inversion is clearly able to give the correct directions of the source current density in addition to its magnitude.

topographic feature of that field is the Cerro Prieto rhyodacitic volcano (Figures 9 and 10). This volcano is less than 700,000 years old and pierces through the Cenozoic sediments filling the Mexicali Valley. The last activity of this volcano was ~14,000–12,000 years ago. The Cerro Prieto geothermal field is one of several high-temperature water-dominated geothermal fields within the Salton Trough (Figure 9). The Salton Trough is a complex rift valley extending between the North American and Pacific plates, forming the landward extension of the Gulf of California, and partially filled by the continental sediments of the delta of the Colorado River.

[41] The Cerro Prieto geothermal field has been used to produce electricity since March, 1973. The Cerro Prieto geothermal plant is the first producing geothermal field in Latin America and the second largest in the world. The field generates several hundreds MW of electric power from reservoirs up to 4000 m deep. The Cerro Prieto geothermal field has been recognized as a complex geological and hydrologic system, and natural flows through this system are controlled by (1) deltaic layered sedimentary units (sands and shales), (2) major faults, (3) buoyancy effects, and (4) the regional hydrological pressure gradient [*Lippmann and Bodvarsson*, 1983]. However, because of the extensive international program of collaborative investigation realized back in the seventies, Cerro Prieto is considered as one of the best studied geothermal fields in North America and it is consequently a suitable target to perform a test of the inversion algorithm presented in section 3 above.

4.1. Hydrology

[42] We first summarize the information useful to embrace a comprehensive model of fluid flow for the Cerro Prieto geothermal field before production began in the seventies. This information includes (1) a description of the main lithostratigraphic units, (2) the location of the reservoirs,

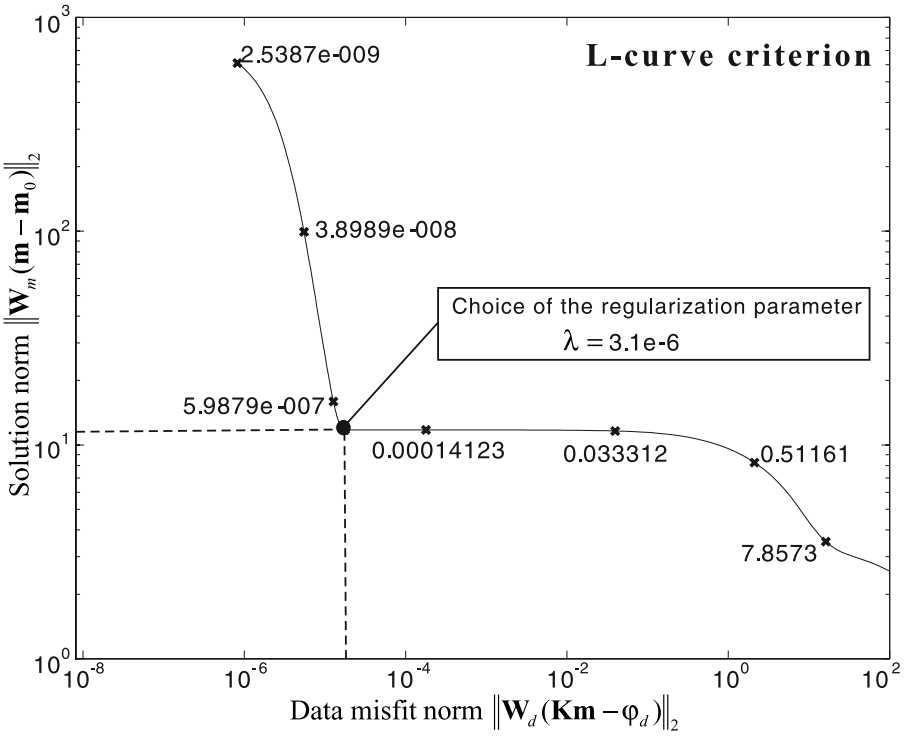

Figure 5. Determination of the regularization parameter using the *L*-curve criterion for the inversion of the synthetic case.

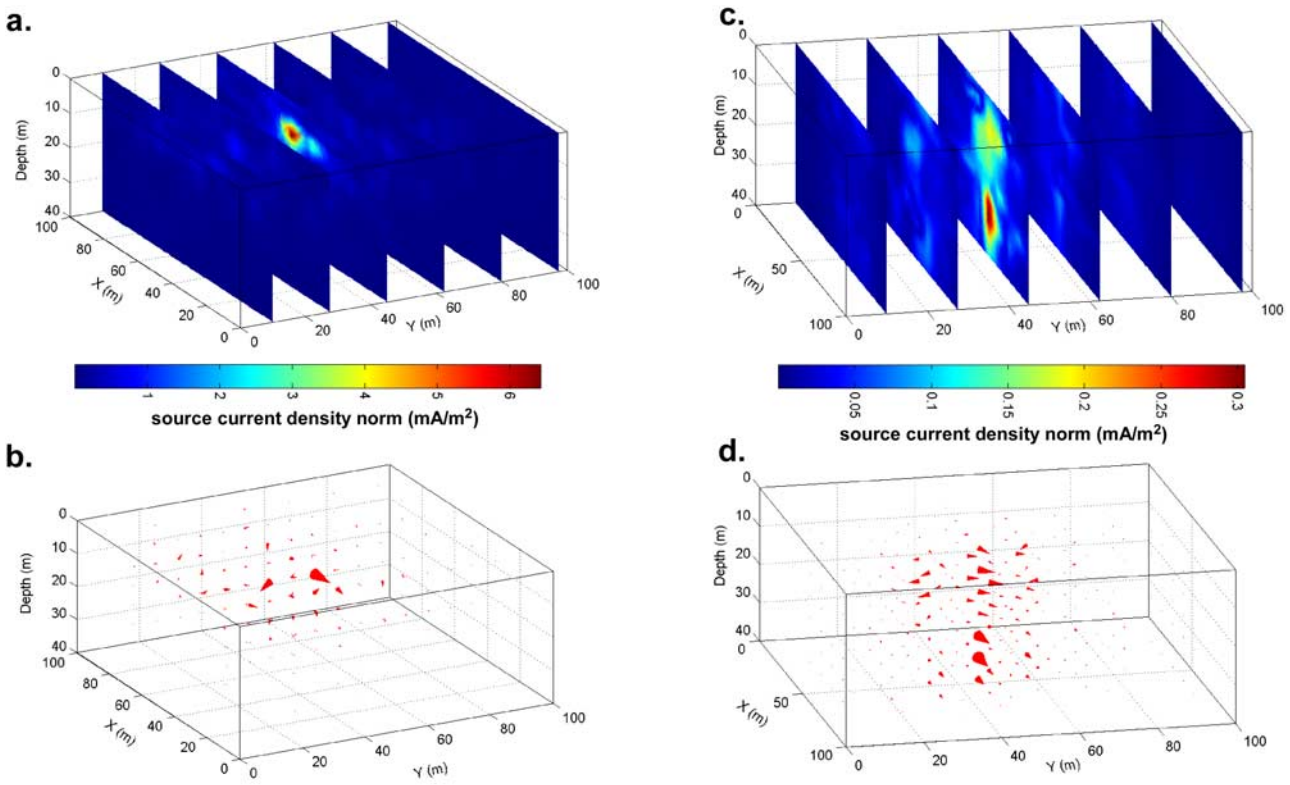

Figure 6. Inversion of the synthetic case for various cases. (a, b) Result of the inversion (amplitude and direction) with a white noise added to the sampled self-potential data (the amplitude of the white noise is equal to 10% of the main self-potential anomaly). The result of the inversion shows that our approach is robust to the presence of white noise (compare with Figure 3). (c, d) Inversion of data without a priori knowledge of the resistivity distribution. Note that, in this case, both the amplitude and the direction of the inverted current density are grossly wrong.

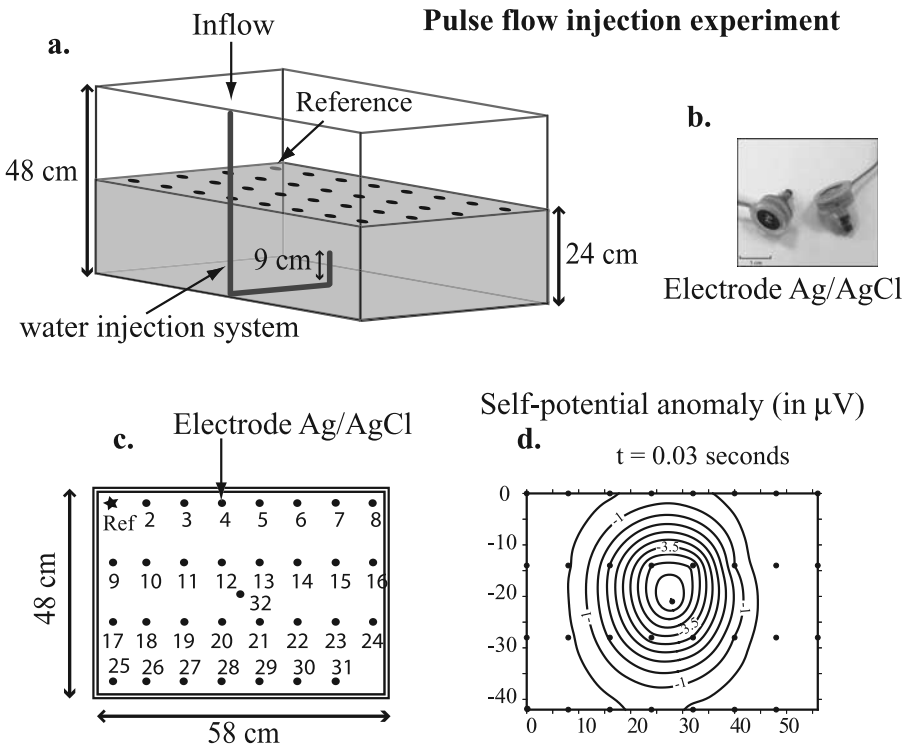

Figure 7. Sketch of the geometry of the sandbox experiment. A total of 32 nonpolarizing electrodes are located at the top surface of the tank, which is partially filled with well-calibrated sand and saturated by a solution of known composition and electrical conductivity. (a) Geometry of the tank. (b) Picture of the self-potential sintered Ag/AgCl electrodes developed by BioSemi. These electrodes are very sensitive, thanks to a built-in amplifier. (c) Sketch of the top surface of the tank showing the position of the electrodes. The electrodes are located at a depth of 3 cm. Ref, position of the reference electrode. Electrode #32 is located just above the inlet/outlet of the capillary. (d) Self-potential anomaly observed on the network of electrodes 30 ms after the pulse injection of water.

natural surface discharge and recharge of the hydrothermal systems and fault networks, (3) the composition of the pore fluid, and (4) the location of heat sources and the dynamic of water flow.

[43] The Cerro Prieto geothermal field can be grossly divided into three main lithostratigraphic units [*de la Peña and Puente*, 1979]. Unit A is composed by unconsolidated and semiconsolidated continental deltaic sediments of undifferentiated Quaternary age. These deltaic sediments show repeated sequences of clays, silts, sands, and gravels and are therefore quite conductive (low electrical resistivity as shown below). The bottom of this unit is formed by coffee-colored shale layers. The thickness of Unit A is between 600 m (well 105) and 2215 m (well Prian-1). Unit B is composed by consolidated continental deltaic sediments of Tertiary age. These sediments are composed of alternating shales, siltstones, and sandstones presenting lenticular bedding. The shales and siltstones are partially metamorphosed. The sandstones are fine grained, usually well-sorted, varying between graywackes and arkoses [*de la Peña and Puente*, 1979]. Core measurements of the porosity range from 0.40 to 0.05 between surface and 2-km depth [*Lyons and van de Kamp*, 1980]. Because of its high clay content, the electrical conductivity of this formation is high. Unit B is discordant on the granitic and metasedimentary Upper Cretaceous basement forming Unit C. This basement has experienced tectonic uplift and subsidence. It is electrically resistive as shown below. The flow of the groundwater goes through these geological units, which are characterized by different electrical conductivity and charge density. Therefore according to equations (15) and (17), the flow of the groundwater is associated with a divergence of the current density, and therefore a source term for the self-potential signals.

[44] The Cerro Prieto geothermal field lies in a tensional zone between the Cerro Prieto and the Imperial transform faults. The extension rate of this pull-apart basin is approximately 10 cm/year [*Elders et al.*, 1983, Figure 9]. The heat source for the hydrothermal system is probably located to the East, near Well NL-1 (Figure 10) in an area where wells have drilled mafic and silicic dikes or sills [*Elders et al.*, 1983]. Such rocks are absent in the central and western parts of the field [*Elders et al.*, 1983]. *Elders et al.* [1983] concluded that the heat source could be a funnel-shaped basalt intrusion, 4 km wide at the top, emplaced at depth of 5 to 6 km about 40,000 to 50,000 years ago in the tensional zone of the pull-apart basin. Deep hot hydrothermal brines recharge the reservoir β through Fault H (Figure 10) [*Lippman et al.*, 1991]. This fault is responsible for some of the seismicity observed in Cerro Prieto field [*Fabriol and Munguía*, 1997].

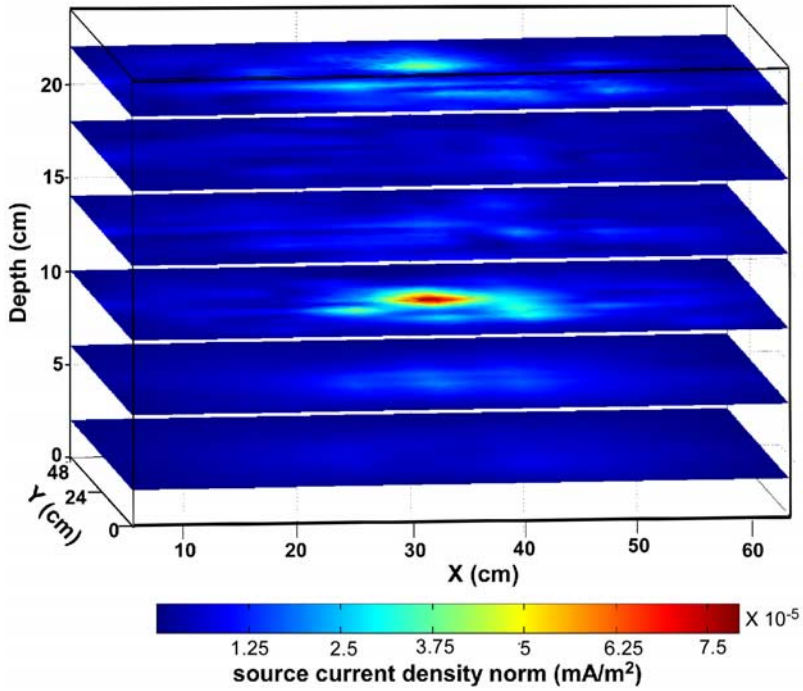

Figure 8. Distribution of the magnitude of the streaming current density. The maximum of the distribution is equal to 8×10^{-5} mA m^{-2}.

[45] Shallow faults like fault H are normal faults in agreement with the extensional nature of the pull-apart basin. The hot fluids flow along reservoir β, and a thermal plume of hot brines close to boiling ascend through a gap in the shale layers. Then they flow toward the West through both reservoirs α and β. The reservoir α and the shallow γ-aquifers are connected by Fault L, and fluid discharges occur from the shallow aquifers in an arc West and Southwest to the field forming hot springs and fumaroles at the surface and shallow zones of temperature reversals (Figures 9, 10, and 11). To the East, a zone of cold water recharge overlies the hot plume discussed previously. Electrical resistivity logs indicate the presence of fresh water at 1500-m deep in well T-366 [*Elders et al.*, 1983]. This requires rapid downward flow (maybe through faults) of cold and low salinity water which recharges the thermal plume. This recharge may also be accompanied by self-sealing because the heated cold CO_2-rich recharge water can precipitate carbonates (predominantly dolomite with subordinate calcite) in the pores of the unconsolidated sediments [*Elders et al.*, 1983].

[46] We need to know the composition, the salinity, and the pH of the groundwater to evaluate the sign of the streaming potential coupling coefficient. The total dissolved solids (primarily NaCl) of the well water vary between 9000 to 37,000 ppm [*Corwin and Hoover*, 1979] with an average value close to 15,000 ppm [*Fausto et al.*, 1981] (note: 1 ppm = 58.443×10^3 C_f/ρ_f, where C_f is the equivalent NaCl solution concentration in mol L^{-1} and 58.443 g mol^{-1} is the molecular mass of NaCl). This leads to salinity in the range 0.15–0.63 mol L^{-1}, with the lowest salinity corresponding to the recharge fluids and the highest to the rising hot plume. *Fausto et al.* [1981] and *Fitterman and Corwin* [1982] considered that the average salinity of the pore fluid is 0.26 mol L^{-1} and 0.43 mol L^{-1}, respectively. The approximate ranges of the concentrations of major components are Cl = 6000–11,000 ppm, SiO_2 = 550–700 ppm, Na = 3000–5500 ppm, K = 500–1000 ppm, Ca = 100–400 ppm, total CO_2 = 10–75 ppm [*Fausto et al.*, 1981]. The pH of the pore fluids is in the range 4.5–5.5, and is controlled by mineral buffer systems such as the feldspar–quartz–muscovite buffer [e.g., *Polster and Barnes*, 1994]. Under these conditions, the streaming potential coupling coefficient is negative as shown by *Revil* [1995] and *Guichet et al.* [2006]. This yields positive values of the volumetric charge density $\overline{Q_v}$. In their numerical simulations, *Goldstein et al.* [1989] used -100×10^{-8} V Pa^{-1} (~ -10 mV m^{-1} if expressed in terms of hydraulic head) for sands and -5×10^{-8} V Pa^{-1} (~ -0.5 mV m^{-1} if expressed in terms of hydraulic head) for shales.

4.2. Self-Potential Anomaly

[47] A map of the self-potential anomalies measured over the Cerro Prieto geothermal field was presented by *Fitterman and Corwin* [1982] from a field survey conducted by *Corwin et al.* [1979; see also *Corwin and Hoover*, 1979; *Corwin and Fitterman*, 1980]. This map covers an area of more than 300 km^2 (Figures 10 and 12). The interpolated data exhibit a dipolar anomaly of ±80 mV with a peak-to-trough distance of ≈7 km with a reference potential ($\varphi(P)$ = 0) chosen at the middle between the two maxima. Note that this choice is arbitrary and only the gradient of self-potential variations along the curvilinear coordinates describing the topography expresses a physical meaning (namely the electrical field).

[48] The self-potential data used in the present study was taken in 1977–1978, which was 4–5 years after the beginning of geothermal power production in 1973. *Goldstein*

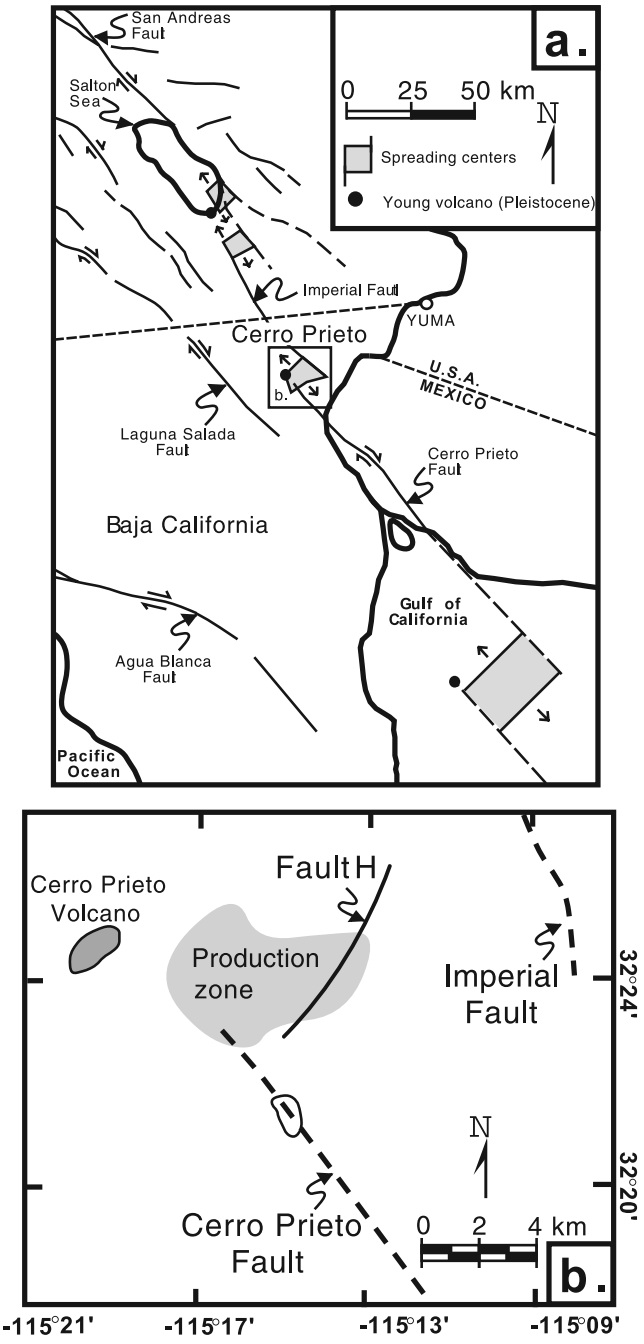

Figure 9. Location of the Cerro Prieto geothermal field. (a) The Cerro Prieto geothermal field is located in Baja California (Mexico). (b) This is a pull-apart basin located between the southeast end of the Imperial Fault and the northern end of the Cerro Prieto Fault.

et al. [1989] reported later the results of a second self-potential survey made in 1988 at Cerro Prieto. They concluded that the anomaly position had shifted about 2 km eastward, which was considered to be due to production. However, at the time of this initial survey (1977–1978), production came from the shallow α-reservoir at a depth of 1 to 1.4 km (discussed above in section 4.1). Thermal recharge was ascending a "sandy gap" in the otherwise impermeable shale O-unit. At the time of the second survey in 1988, the situation was very different. Production has been greatly expanded eastward with most fluids produced from the deeper β-reservoir. Thermal recharge was guided, in part, by the H-fault. This was identified as the main reason for the shift of the self-potential anomaly [*Goldstein et al.*, 1989]. Therefore the disturbance created by production was much smaller in 1978 than it was in 1988.

[49] A second point is the effect of the metallic casing of the well in generating electroredox effect with self-potential anomalies of strong amplitudes. A theory of this effect has been presented recently by *Castermant et al.* [2008]. The source of the current density is localized near the piezometric surface intersected by the metallic casing where the vertical gradient of the redox potential is the highest. At Cerro Prieto, the aquifer is located at shallow depths, therefore the redox effect associated with the corrosion of the metallic casing of the boreholes produced only localized self-potential signals (see for a field example *Rizzo et al.* [2004]). Production of water in boreholes with metallic casing can also be the source of self-potential anomalies as modeled by *Ishido et al.* [1989] and *Titov et al.* [2005b]. However, because production was performed in the shallow α-reservoir, we believe that production produced only localized (<2 km) self-potential anomalies.

[50] Consequently, we will regard the self-potential distribution from the 1977–1978 survey as being representative of the natural steady state condition of flow. To explain this self-potential anomaly, *Fitterman and Corwin* [1982] used a thermo-electrostatic source mechanism located within a fault separating regions of different thermo-electric properties. The thermo-electrostatic mechanism is very different from the electrokinetic phenomena envisioned in the present paper. The ionic thermo-electrostatic potential is an ionic analog of the electronic Thompson effect occurring at the contact between two different metals in the presence of a temperature gradient perpendicular to their contact.

[51] We see three problems with the approach used by *Fitterman and Corwin* [1982]: (1) No fault of the predicted extent (9.9 ± 0.4 km) is observed at the predicted location, i.e., in between the positive and the negative peaks of the self-potential anomaly. The L fault (see Figure 17 of *Rodríguez et al.* [2000]) has roughly the same orientation than the predicted fault but its extension is much smaller (<4 km) (see Figure 6 of *Fitterman and Corwin* [1982]). (2) The top of the source is located at 1.3 ± 0.2 km and its vertical extent is 11 ± 3 km. This last depth seems unlikely because the basement is located at much shallower depths (3 to 5 km) as discussed in the previous section. (3) The thermo-electric coupling coefficient needed by *Fitterman and Corwin* [1982] to explain the dipolar anomaly of Figure 12 is about one order of magnitude higher than those reported in the literature for sandy and clayey sediments (see a review in *Revil* [1999]). The thermo-electrostatic effect would generate only an electrical self-potential anomaly one order of magnitude smaller than observed at Cerro Prieto. The thermo-electric explanation is then problematic. *Sill* [1983] found a similar difficulty with the thermoelectric effect to explain the dipolar potential anomaly observed at Red Hill Hot Spring in Utah.

[52] *Corwin and Fitterman* [1980] mentioned that the source of the observed self-potential signals could be also due to the upward of fluid flow along a fault zone across

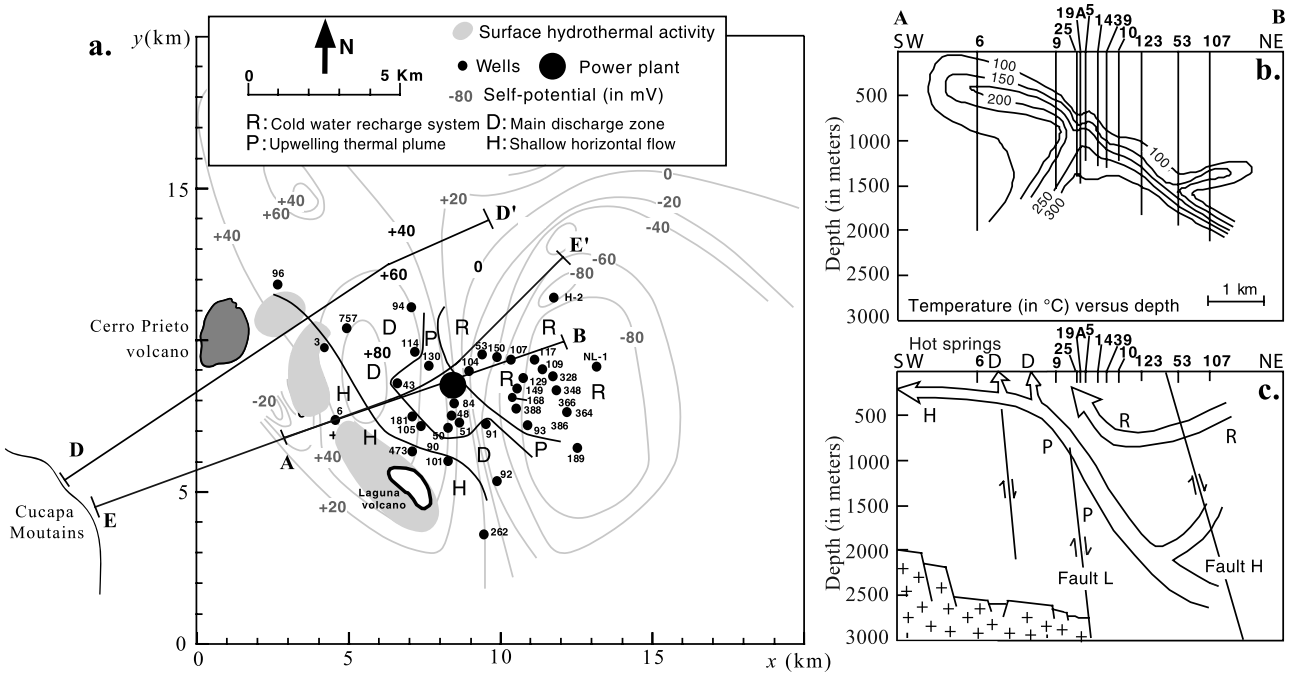

Figure 10. Flow pattern of the Cerro Prieto geothermal field. (a) The Cerro Prieto geothermal field can be divided into regions with different patterns of mineral zones and flow regimes in 1973. R, recharge zone; P, thermal plume zone; D, discharge zone; H, horizontal flow zone [modified from *Elders et al.*, 1983]. The location of some of the wells is indicated by the filled circles. The profiles EE′ and DD′ are the DC resistivity (dipole–dipole) profiles. The large box corresponds to the area where the self-potential investigations have been carried by *Fitterman and Corwin* [1982] (see Figure 9). Their self-potential map is shown in light grey. (b) Temperature distribution based on the calcite–water oxygen isotope geothermometer [modified from *Elders et al.*, 1983]. The temperature distribution shows a broad area of temperature inversion in the southwest due to a zone of horizontal hot brines flow. (c) Flow regime [modified from *Elders et al.*, 1983]. R, recharge zone; P, thermal plume zone; D, discharge zone; H, horizontal flow zone. We add the faults and the position of the basement.

which there is a change of the streaming potential coupling coefficient. *Fitterman and Corwin* [1982] wrote, in their conclusion, that "we have not ruled out the possibility that the observed spontaneous potential anomaly is generated by a streaming potential mechanism. Modeling using this type of a source mechanism would be helpful in determining the cause of the SP anomaly." Later, *Goldstein et al.* [1989] demonstrated that the thermoelectric effect was much too low to explain the self-potential anomalies observed at Cerro Prieto. They used the finite difference code developed by Sill to develop a forward model showing that the streaming current assumption can quantitatively explain the self-potential anomalies and the observed variations in the self-potential field between the 1978 and the 1988 surveys. Recent works [e.g., *Garg et al.*, 2007] also favor the streaming potential explanation rather than the thermo-

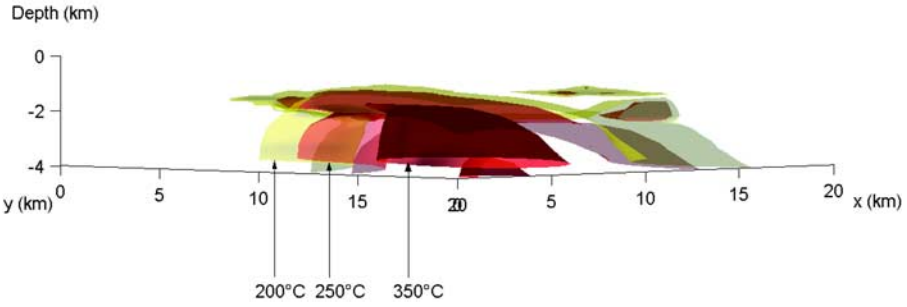

Figure 11. Three-dimensional temperature anomaly showing the position of the hydrothermal plume rising toward the ground surface (see also Figure 10). Temperature data are based on the calcite–water oxygen isotope geothermometer [see *Elders et al.*, 1983]. Temperatures above 350°C result from the interpolation of the data. The side view is taken from the southwest, where the plume of hot water discharges. The box (20 × 20 km) is the one shown in Figure 10a.

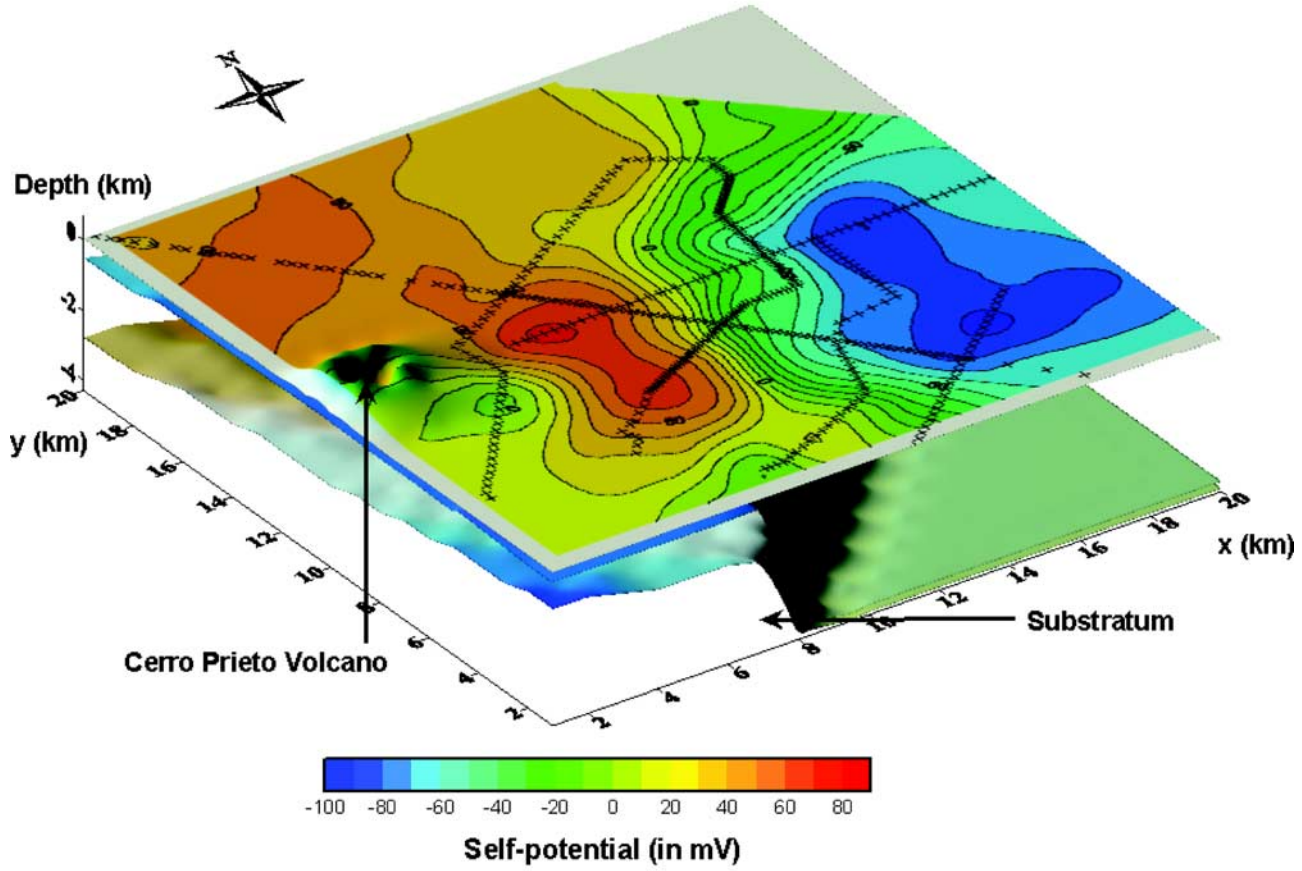

Figure 12. Self-potential contours at the ground surface of the Cerro Prieto geothermal field [data from *Fitterman and Corwin*, 1982]. The location of the self-potential measurements is indicated by the crosses. The self-potential map exhibits a dipolar anomaly with a peak-to-peak amplitude of 160 mV. The position of the substratum (granite and metasedimentary upper Cretaceous basement) is determined from borehole data plus the seismic and deep resistivity surveys. The size of the model used in this study is 20 × 20 × 4 km. The position of the box (20 × 20 km) is shown in Figure 10a.

electric coupling to explain the self-potential anomalies over geothermal fields.

4.3. Electrical Resistivity Distribution

[53] In order to invert the self-potential data, we need the three-dimensional distribution of the electrical resistivity below the area covered by the self-potential measurements. Our goal was therefore to generate a three-dimensional block of electrical resistivity data with an extent of 400 km^2 at the ground surface and extending to a depth of 4 km below the area where the self-potential survey was carried out (see the block 20 × 20 km delimited in Figure 10a). Several large scale resistivity profiles were obtained by *Wilt and Goldstein* [1981] (see for example the profiles EE′ and DD′ in Figure 10). Acquisition of large resistivity pseudosections are customarily made with harmonic currents (>1 A) and large offsets of the electrodes [see *Storz et al.*, 2000]. We have inverted these large pseudosections of apparent resistivity data with the commercial software RES2DINV [*Loke and Barker*, 1996]. The result of the inversion is shown in Figure 13. Once inverted, the resistivity data give an idea of the large scale resistivity structure of the Cerro Prieto geothermal field. The volume shown in Figure 12 is discretized with a total of 6400 elements. The size of each element is $\delta x = \delta y =$ 1 km and a thickness of 250 m in δz (x, y, z are Cartesian coordinates with z in the vertical direction). Each block has a given mean lithology (sandstone, shale, or granite) and a mean temperature.

[54] The lithology is derived from two geological cross-sections made over the Mexicali valley (see Figures 5 and 6 from *Manon et al.* [1977]). These sections are oriented NW–SE for the former and SW–NE for the second, length 7 km and a depth of 4 km. As explained above, the Mexicali valley has a granitic basement and is filled with sandstones (>3 km) and a superficial layer of shales (1 km in thickness). The temperature has been interpolated from the temperature obtained in boreholes (e.g., Figures 10 and 11). To build our resistivity model (shown in Figure 14), we use the following values of the resistivity at 25°C:1 Ω m for the shale, 20 Ω m for the sandstone, 300 Ω m for the fractured granite, and 2 Ω m for the alluvial cones. The temperature dependence of the resistivity of these units is taken from *Revil and Pezard* [1998]. The cells for which no data are available were interpolated with an ordinary kriging algorithm.

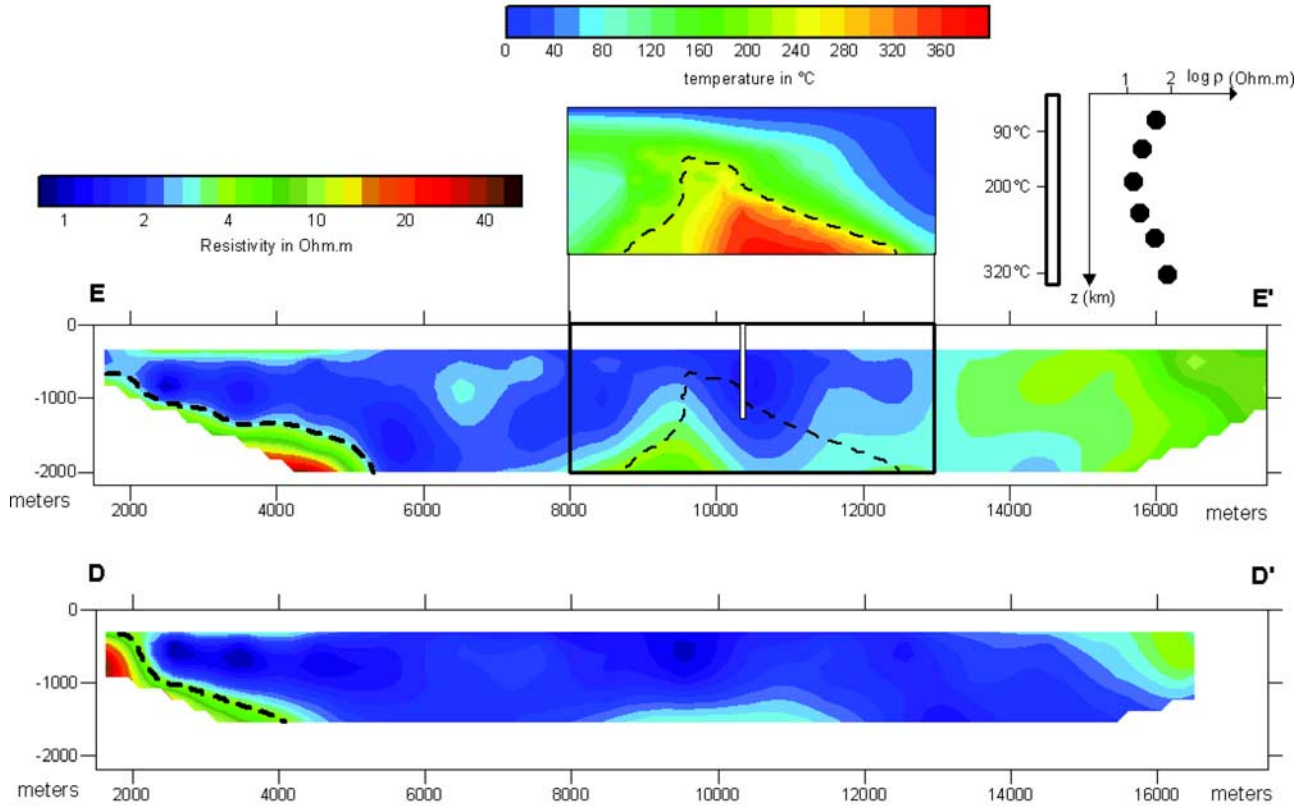

Figure 13. Two-dimensional electrical resistivity tomograms (profiles EE′ and DD′, see position in Figure 8) inverted with RES2DINV [*Loke and Barker*, 1996]. The resistive structures (on the left-hand sides of the profiles) correspond to the granitic and metasedimentary upper Cretaceous substratum. The resistivity of the substratum is higher than 40 Ω m. Between the ground surface and the substratum, the resistivity is comprised between 1 and 3 Ω m.

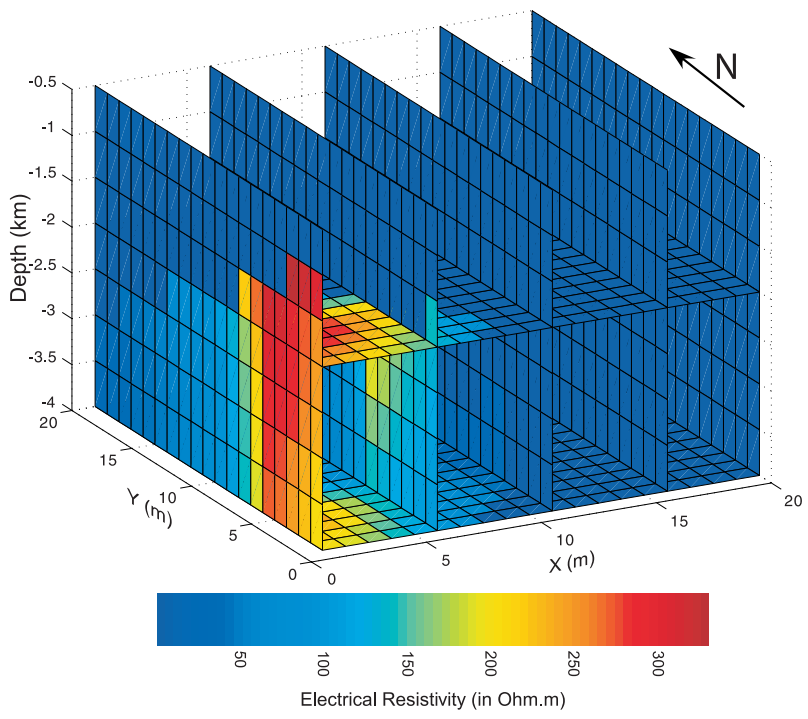

Figure 14. Distribution of the electrical resistivity used for the inverse problem of the self-potential data.

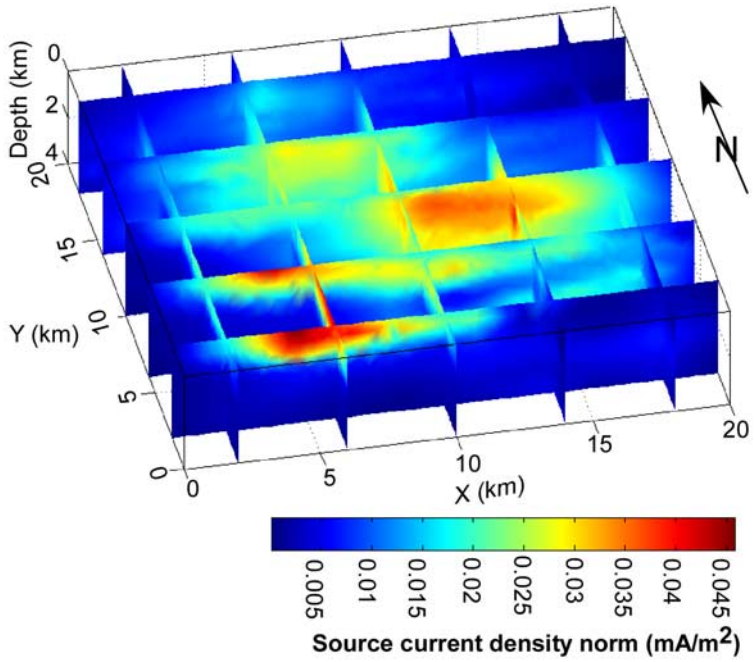

Figure 15. Magnitude of the inverted three-dimensional streaming current source density (expressed in mA m^{-2}) accounting for the resistivity distribution shown on Figure 14. The result of the inversion shows a shallow source in the western part of the system and a source located at greater depths (2 km) in the central part of the system. These results are consistent with the flow pattern known to occur in the Cerro Prieto geothermal field.

4.4. Inversion of Self-Potential Data

[55] The final step is to take the self-potential and resistivity data to invert the three-dimensional distribution of the electrical current density in the geothermal field (Figures 15 to 20). In Figure 15, we plot the intensity of the inverted source current density accounting for the resistivity model shown in Figure 14. To make a comparison, we also inverted the same source current density when the resistivity is taken as constant (5 Ω m). When the

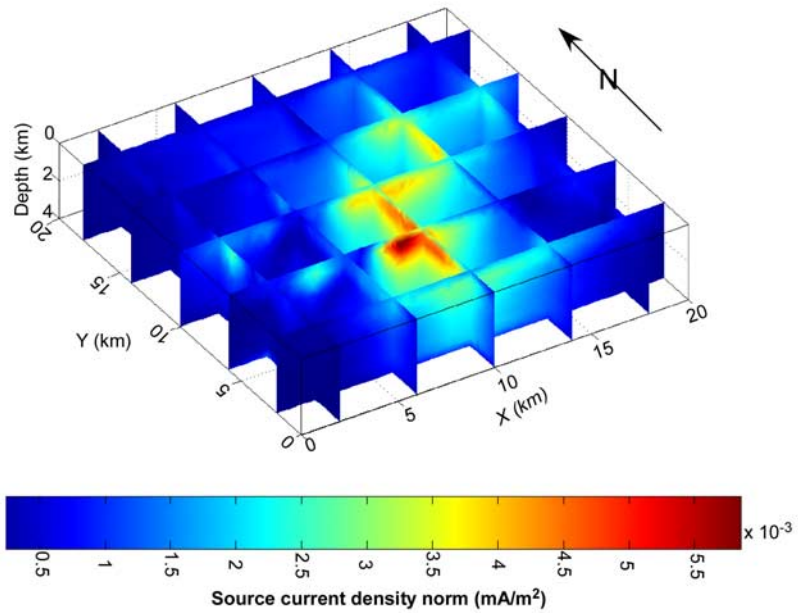

Figure 16. Magnitude of the inverted three-dimensional streaming current source density (expressed in mA m^{-2}) assuming a constant resistivity. The result is not consistent with the flow pattern known to occur in the Cerro Prieto geothermal field.

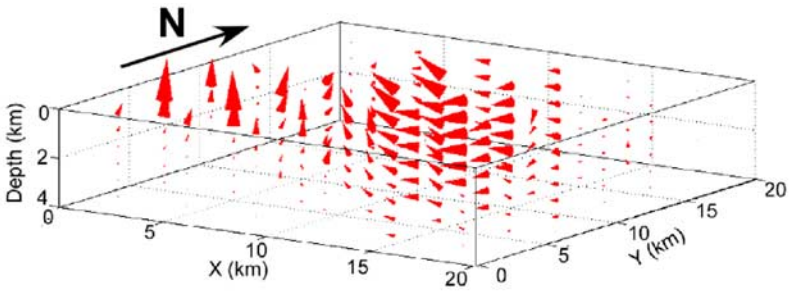

Figure 17. Three-dimensional inversion of the direction of the streaming current density from self-potential and resistivity data. The size of the arrows is proportional to the magnitude of the current density. As the Darcy velocity is proportional to the current density, the direction of the current density is also equal to the direction of the seepage velocity associated with the hydrothermal flow field. We see clearly the area of hydrothermal discharge in the southwest part of the investigated area (see areas D and H in Figure 10a).

resistivity is taken constant, the inverted current density pattern does not match the thermal plume (both the deep of it and the discharge area in the south-west part of the investigated area, see Figure 16). As discussed below, the inverted pattern of the source current density is consistent with the flow pattern of the Cerro-Prieto geothermal field only when resistivity is properly taken into account. We let a sensitivity analysis associated with the resistivity distribution for a future work but the distribution of the resistivity is therefore an important ingredient to invert the self-potential data.

[56] In the central portion of the investigated system, the source current density is localized at depths between 0 and 2 km. In the Western part of the system, the source current density is located at shallow depths (less than few hundreds meters). The direction of the inverted source current density, accounting for the resistivity distribution, is shown in Figure 17. These directions are in good agreement with the flow field shown in Figure 10 and with the fluid flow model discussed by *Rodríguez et al.* [2000] prior the exploitation of the geothermal field in March 1973. In the model of *Corwin and Fitterman* [1980], the asymmetry of the self-potential anomaly observed at the ground surface is considered to be due to a change of the electrical conductivity across their assumed fault plane. They also mentioned that the asymmetry of the self-potential anomaly could be due to a nonvertical dip angle of the fault zone in which the source is embedded. In the present case, the asymmetry of the self-potential anomaly is due to the pattern of groundwater flow in the system, which is partly controlled by the presence of a fault system in the central part of the system, and to the resistivity distribution of the geothermal field.

[57] The fit of the self-potential data is shown in Figure 18. Because the standard deviations on the data is close to 20 mV (likely because local heterogeneity of the resistivity distribution near the surface), it is not surprising to see the fit of the self-potential data.

[58] The contour of the inverted streaming current density (with a critical value equal to 0.02 mA m^{-2}) is shown on Figure 19. The shape of the electrokinetic (source) current density at depth evidences a rising plume of groundwater flow. This plume is fairly consistent with the thermal plume shown on Figure 11 before the production of the geothermal field and the updated fluid flow model presented by *Rodríguez et al.* [2000] (their Figures 17 to 19). In this report, the authors discussed the initial flow model for the Cerro Prieto geothermal field and its evolution since 1973. The main surface manifestations of the geothermal system are found in the Western part of the system (in the Laguna volcano area [see *Lippman et al.*, 1991]). In this area hot fluids form a large shallow aquifer, which discharges the geothermal fluids toward the surface. This is in agreement with the flow model inferred from the self-potential data (see Figures 15 and 19). In the Eastern part of the system, the flow model proposed by *Rodríguez et al.* [2000] indicates that before 1973, there was no flow of the groundwater in the first two kilometers below the ground surface. This is also in agreement with the flow model inferred from the self-potential data.

[59] To visualize this consistency, we plot in Figure 20 the temperature versus the norm of the source current

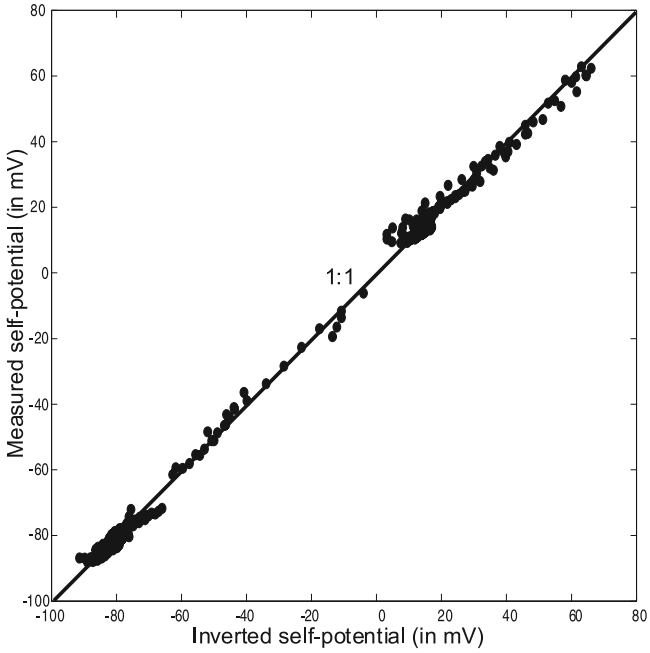

Figure 18. Comparison between the measured self-potential data (275 stations) and the self-potentials resulting from the inverted current density (R^2 = 0.9960).

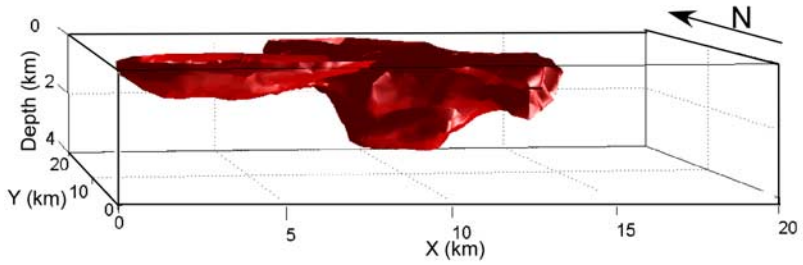

Figure 19. Contour of the inverted streaming current density (the surface corresponds to a threshold value of 0.02 mA m^{-2}). This anomaly provides information regarding the extension of the hydrothermal plume (see Figure 11).

density. In the central portion of the system (Y = 10 km, $X \in$ = (1, 20) km, and Z = 3 km), there is a good agreement between the position of the thermal anomaly and the inverted source current density. A second profile (corresponding to the coordinates Y = 15 km, $X \in$ (1, 20) km, Z = 3 km) shows only a fair agreement between the intensity of the electrokinetic current density and the temperature. This shows that the inversion of self-potential data can be a useful nonintrusive method to determine the pattern of the groundwater flow at large scales. This determination could be improved by a joint inversion of the self-potential and borehole temperature data. This approach appears promising because of the obvious complementarity of the two types of data.

5. Concluding Statements

[60] Self-potential signals can be used to observe remotely the pattern of groundwater flow (or changes in this pattern) or to detect the occurrence of fracturing at depth in water infiltrated rocks. We proposed a three-dimensional algorithm to reconstruct the pattern of fluid flow in a geological system from the inversion of self-potential data or to locate fracturing events. Our inversion algorithm uses Tikhonov regularization of the inverse problem and the L-shape method to determine the regularization parameter. Our algorithm used constraints that are specific to the problem under consideration (fluid flow or fracturing). These constraints are set up in the form of a priori information regarding the inverse problem. Application to the data of Cerro Prieto shows that the inverted current density at depth is in good agreement with the position of the plume of hydrothermal groundwater resulting from the interpolation of temperature data obtained independently in a set of boreholes spreading over the geothermal field.

[61] In a future contribution, we will propose a joint inversion modeling of self-potential and thermal data to invert the pattern of groundwater. We will also address the

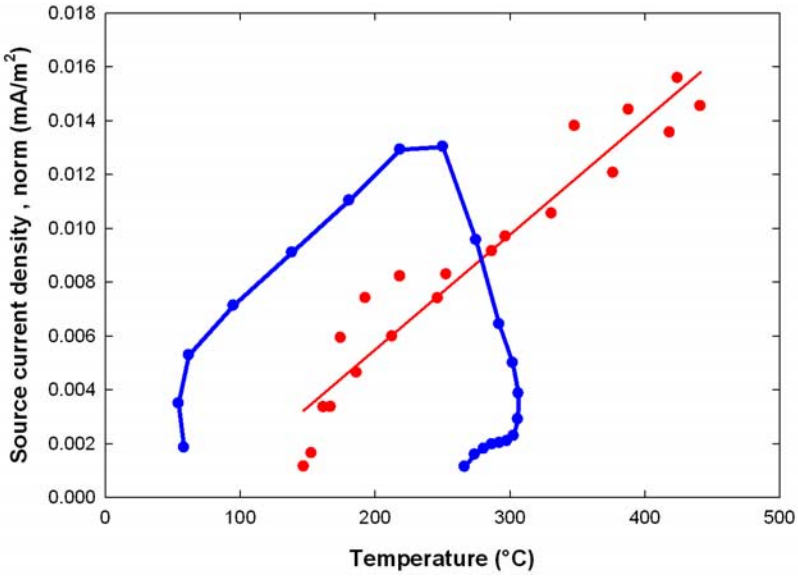

Figure 20. Comparison between the ground truth temperature data obtained in boreholes and resulting from the interpolation of in situ estimates (see Figure 11) and the norm of the source current density resulting from the inversion of the self-potential data. The profile in red corresponds to the profile of coordinates Y = 10 km, $X \in$ [1:1:20] km, and Z = 3 km (see position on Figure 12). This profile shows a linear trend between the electrokinetic source current density and the temperature. The second profile (in blue) corresponds to the coordinates Y = 15 km, $X \in$ (1, 20) km, Z = 3 km. This second profile shows a linear portion at temperatures below 250°C and a nonlinear portion at higher temperatures.

problem of the sensitivity of the inverted current density distribution to the knowledge of the resistivity distribution of the medium.

Appendix A: Determination of the Kernel

[62] Elementary sources of current, in a conductive medium, can be represented as dipoles. The electrical potential resulting from a collection of dipoles is the sum of the electrical potential distributions resulting from each dipole taken separately as a result of the superposition principle. The Poisson equation $\nabla \cdot (\sigma \nabla \varphi) = \nabla \cdot \boldsymbol{j}_S$ corresponds to a linear transformation between the source current density $\boldsymbol{j}_S$ and the resulting self-potential field φ. To close the problem, we need to specify boundary conditions for the electrical potential and the current density at each interfaces ($\boldsymbol{n} \cdot \boldsymbol{j} = 0$ at the ground surface) where $\boldsymbol{j}$ is the total current density. We can introduce the Green function $\boldsymbol{G}(M, P)$ connecting the source current density at point M and the electrical potential at point P: $\varphi(P) = \boldsymbol{G}(M, P) \cdot \boldsymbol{j}_S(M)$. We consider a collection of m elementary source (in three-dimensional, there are $3m$ components of the current density to retrieve) and n observation stations P. In the study of self potential signals, the inverse problem is undermined because $3\ m \gg n$. In this case, the potential at any station P is given by a convolution product between the kernel $\boldsymbol{K}$ and the source current density at each source point, see equation (18). Each element of $\mathbf{K}$ is a Green function:

$$\mathbf{K} = \begin{bmatrix} G_x^{11} & G_y^{11} & G_z^{11} & \cdots & G_x^{1m} & G_y^{1m} & G_z^{1m} \\ \vdots & \vdots & \vdots & \ddots & \vdots & \vdots & \vdots \\ G_x^{11} & G_y^{11} & G_z^{11} & \cdots & G_x^{nm} & G_y^{nm} & G_z^{nm} \end{bmatrix}. \quad \text{(A1)}$$

The matrix $\mathbf{K}$ depends only on the number of observation station, the number of elementary sources, and the distribution of the electrical resistivity of the system. When computing the elements of $\mathbf{K}$, one has to remember that the electrical potential is determined relatively to a reference electrode located somewhere in the system. By definition, the electrical potential at the reference station is taken equal to zero and this condition should be fulfilled for all the elements of $\mathbf{K}$ by removing the potential computed at this location from the self-potential distribution determined over the field. To determine the elements of the kernel, we consider that each elementary cell used to discretize the system has a uniform electrical resistivity and each elementary current density can be written as $\boldsymbol{j}_S(M) = \boldsymbol{m}\delta(M)$ where $\boldsymbol{m}$ is the dipole moment, $\delta(\boldsymbol{r})$ is the Dirac function, and M is the position of the elementary source. For all these elementary dipoles, we solve the Poisson's equation.

[63] The matrix $\mathbf{K}$ can be written with simple analytical functions only in the case for which the electrical resistivity is uniform all over an infinite system (or for very simple geometries using for example the image method). In this case, we have

$$G_{x,y,z}^{ij} = \frac{1}{4\pi\sigma} \frac{\left(r_{Pi} - r_{Mj}\right)_{x,y,z}}{\left|r_{pi} - r_{Mj}\right|^3}, \quad \text{(A2)}$$

with $i \in \{1, \ldots, n\}$, $j \in 1, \{1, \ldots, m\}$ and σ is the electrical conductivity of the medium. According to equation (A2), it is clear that $G_{x,y,z}^{ij}$ is large for sources located in the vicinity to the ground surface. To counteract this effect, it can be necessary to introduce the weighting matrix given, in the general case, by equation (14).

[64] In the cases reported in this paper, we are dealing with heterogeneous resistivity distributions. In this case, the elementary Green functions are computed numerically, using the finite element code Comsol Multiphysics 3.3 (see *Arora et al.* [2007] for an example where a surface distribution of dipoles lying over the water table is used to compute the self-potential response). The determination of the kernel is the most computationally intensive step in self-potential tomography.

[65] **Acknowledgments.** This work is supported by the French National Research Council (CNRS), the GDR-FORPRO, ANR-Projects POLARIS, ERINOH, and the French National Agency for Radioactive Waste Management (ANDRA). We thank Nicolas Florsch and Niklas Linde for fruitful discussions. We thank the Associate Editor, Douglas Schmitt, and two anonymous referees for their very useful comments of the paper. Terry Young is thanked for his strong support at the Colorado School of Mines. This work is dedicated to the memory of R.F. Corwin for his very fruitful contributions to the study of self-potential signals.

References

Aizawa, K., et al. (2005), Hydrothermal system beneath Mt. Fuji volcano inferred from magnetotellurics and electric self-potential, *Earth Planet Sci. Lett.*, *235*, 343–355.

Arora, T., A. Revil, N. Linde, and J. Castermant (2007), Non-intrusive determination of the redox potential of contaminant plumes using the self-potential method, *Contamin. Hydrol.*, *92*, 274–292.

Aubert, M., and Q. Y. Atangana (1996), Self-potential method in hydrogeological exploration of volcanic areas, *Ground Water*, *34*, 1010–1016.

Bedrosian, P. A., M. J. Unsworth, and M. J. S. Johnston (2007), Hydrothermal circulation at Mount St. Helens determined by self-potential measurements, *J. Volcanol., Geotherm. Res.*, *160*, 137–146.

Black, W. E., and R. F. Corwin (1985), Application of self-potential measurements to the delineation of groundwater seepage in Earth-fill embankments, *Geophysics*, *50*(2), 283–283.

Bogoslovsky, V. V., and A. A. Ogilvy (1973), Deformations of natural electric fields near drainage structures, *Geophys. Prospect.*, *21*, 716–723.

Bolève, A., A. Crespy, A. Revil, F. Janod, and J. L. Mattiuzzo (2007a), Streaming potentials of granular media: Influence of the Dukhin and Reynolds numbers, *J. Geophys. Res.*, *112*, B08204, doi:10.1029/2006JB004673.

Bolève, A., A. Revil, F. Janod, J. L. Mattiuzzo, and A. Jardani (2007b), Forward modeling and validation of a new formulation to compute self-potential signals associated with ground water flow, *Hydrol. Earth Syst. Sci.*, *11*, 1–11.

Castermant, J., C. A. Mendonça, A. Revil, F. Trolard, G. Bourrié, and N. Linde (2008), Redox potential distribution inferred from self-potential measurements during the corrosion of a burden metallic body, *Geophys. Prospect.*, *56*, 269–282, doi:10.1111/j.1365-2478.2007.00675.x.

Corwin, R. F. (1985), The self-potential method and its engineering applications - an overview, *Geophysics*, *50*(2), 282–282.

Corwin, R. F., and D. V. Fitterman (1980), Geological interpretation of self-potential data from the Cerro Prieto geothermal field, Report LBL 9544, Conf. 1910166-12, Cerro-Prieto 17, Mexican-American cooperative program at the Cerro Prieto geothermal field, February 1980.

Corwin, R. F., and D. B. Hoover (1979), The self-potential method in geothermal exploration, *Geophysics*, *44*, 226–245.

Corwin, R. F., H. F. Morrison, and M. Y. Chang (1976), Monitoring earthquake-related variations of electrical resistivity and self-potential on San-Andreas fault, *Trans. Am. Geophys. Union*, *57*(4), 288–288.

Corwin, R. F., H. F. Morrison, S. Diaz, and J. Rodriguez (1979), Self-potential studies at the Cerro Prieto geothermal field, September 20–22, 1978, San Diego, Lawrence Berkeley Lab. Report LBL-7098, pp. 204–210.

Corwin, R. F., G. T. Demoully, R. S. Harding, and H. F. Morrisson (1981), Interpretation of self-potential survey results from the East Mesa geothermal field, California, *J. Geophys. Res.*, *86*(B3), 1841–1848.

Crespy, A., A. Revil, N. Linde, S. Byrdina, A. Jardani, A. Bolève, and P. Henry (2008), Detection and localization of hydromechanical disturbances in a sandbox using the self-potential method, *J. Geophys. Res.*, *113*, B01205, doi:10.1029/2007JB005042.

de la Peña, L. A. and C. I. Puente (1979), The geothermal field of Cerro Prieto, in *Geology and Geothermics of the Salton Trough: Riverside*, Report UCR/IGPP-79/23, edited by W. A. Elders, pp. 20–35, Univ. of Calif., Inst. of Geophysics and Planetary Phys, Geological Society of America.

Elders, W. A., D. K. Bird, A. E. Williams, and P. Schiffman (1983), Hydrothermal flow regime and magmatic heat source of the Cerro Prieto geothermal system, Baja California, Mexico, *Geothermics*, *13*, 27–47.

Fabriol, H., and L. Munguía (1997), Seismic activity at the Cerro Prieto geothermal area (Mexico) from August 1994 to December 1995, and its relationship with tectonics and fluid exploitation, *Geophys. Res. Lett.*, *24*(14), 1807–1810.

Fausto, J. J., S. M. E. Jimenez, and P. I. Esquer (1981), Estado actual de los estudios sobre geoquímica hidróthermal en Cerro Prieto, in *Proceedings of the Third Symposium on the Cerro Prieto Geothermal Field, March 1981*, pp. 188–220, San Francisco, Lawrence Berkeley Lab. Rep. LBL-1197.

Finizola, A., S. Sortino, J.-F. Lénat, and M. Valenza (2002), Fluid circulation at Stromboli volcano (Aeolian Islands, Italy) from self-potential and CO_2 surveys, *J. Volcanol. Geotherm. Res.*, *116*, 1–18.

Finizola, A., S. Sortino, J.-F. Lénat, M. Aubert, M. Ripepe, and M. Valenza (2003), The summit hydrothermal system of Stromboli. New insights from self-potential, temperature, CO_2 and fumarolic fluid measurements. Structural and monitoring implications, *Bull. Volcanol.*, *65*, 486–504, doi:10.1007/s00445-003-0276-z.

Finizola, A., J.-F. Lénat, O. Macedo, D. Ramos, J. C. Thouret, and F. Sortino (2004), Fluid circulation and strcutural discontinuities inside Misti volcano (Peru) inferred from self-potential measurements, *J. Volcanol. Geotherm. Res.*, *135*, 343–360.

Fitterman, D. V. (1984), Thermoelectrical self-potential anomalies and their relationship to the solid angle subtended by the source region, *Geophysics*, *49*, 165–170.

Fitterman, D. V., and R. F. Corwin (1982), Inversion of self-potential data from the Cerro Prieto geothermal field, Mexico, *Geophysics*, *47*, 938–945.

Frank, E. H., and A. J. Grodzinsky (1987), Cartilage electromechanics: II. A continuum model of cartilage electrokinetics and correlation with experiments, *J. Biomech.*, *20*, 629–639.

Garg, S. K., J. W. Pritchett, P. E. Wannamaker, and J. Combs (2007), Characterization of geothermal reservoirs with electrical surveys, *Geothermics*, *36*, 487–517.

Gex, P. (1993), Electrofiltration measurements on the Frasse landslide, the Pre-Alps of western Switzerland, *Hydrogéologie*, *3*, 239–246.

Goldstein, N. E., S. Halfman, R. F. Corwin, and J. Martinez (1989), Self-potential anomaly changes at the East Mesa and Cerro Prieto geothermal fields, in *Proceedings 14th Workshop on Geothermal Reservoir Engineering*, pp. 145–153, SGP-TR-122, Stanford Univ., Stanford, Calif., 24–26 January.

Guichet, X., L. Jouniaux, and N. Catel (2006), Modification of streaming potential by precipitation of calcite in a sand-water system: Laboratory measurements in the pH range from 4 to 12, *Geophys. J. Int.*, *166*, 445–460.

Haber, E., and D. W. Oldenburg (2000), A GCV-based method for nonlinear inverse problems, *Comput. Geosci.*, *4*, 41–63.

Hansen, P. C. (1998), *Rank-Deficient and Discrete Ill-Posed Problems: Numerical Aspects of Linear Inversion*, 247 pp., Soc. for Industrial and Applied Mathematics, Philadelphia, Pa.

Hase, H., T. Hashimoto, S. Sakanaka, W. Kanda, and Y. Tanaka (2005), Hydrothermal system beneath Aso volcano as inferred from self-potential mapping and resistivity structure, *J. Volcanol. Geotherm. Res.*, *143*, 259–277.

Huang, Q. (2002), One possible generation mechanism of co-seismic electric signals, *Proc. Jpn. Acad.*, *78*(7B), 173–178.

Huang, Q., and T. Liu (2006), Earthquakes and tide response of geoelectric potential field at the Niijima station, *Chin. J. Geophys.*, *49*(6), 1745–1754.

Huygue, J. M., R. Van Loon, and F. T. P. Baajens (2004), Fluid-solid mixtures and electrochemomechanics: The simplicity of Lagrangian mixture theory, *Comput. Appl. Math.*, *23*(2–3), 235–258.

Ishido, T. (1989), Self-potential generation by subsurface water flow through electrokinetic coupling, *Lect. Notes Earth Sci.*, *27*, 121–133.

Ishido, T. (2004), Electrokinetic mechanism for the "W"-shaped self-potential profile on volcanoes, *Geophys. Res. Lett.*, *31*, L15616, doi:10.1029/2004GL020409.

Ishido, T., and H. Mizutani (1981), Experimental and theoretical basis of electrokinetic phenomena in rock-water systems and its application to geophysics, *J. Geophys. Res.*, *86*, 1763–1775.

Ishido, T., T. Kikuchi, and M. Sugihara (1989), Mapping thermally driven upflows by the self-potential method, in *Hydrogeological Regimes and Their Subsurface Thermal Effects*, *Geophys. Monogr.*, *47*, IUGG vol. 2, edited by A. E. Beck, G. Garven, and L. Stegena, pp. 151–158, AGU, Washington, D. C.

Jardani, A., J. P. Dupont, and A. Revil (2006a), Self-potential signals associated with preferential ground water flow pathways in sinkholes, *J. Geophys. Res.*, *111*, B09204, doi:10.1029/2005JB004231.

Jardani, A., A. Revil, F. Akoa, M. Schmutz, N. Florsch, and J. P. Dupont (2006b), Least-squares inversion of self-potential (SP) data and application to the shallow flow of the ground water in sinkholes, *Geophys. Res. Lett.*, *33*, L19306, doi:10.1029/2006GL027458.

Jardani, A., A. Revil, A. Bolève, A. Crespy, J. P. Dupont, W. Barrash, and B. Malama (2007), Tomography of the Darcy velocity from self-potential measurements, *Geophys. Res. Lett.*, *34*, L24403, doi:10.1029/2007GL031907.

Jouniaux, L., and J. P. Pozzi (1995), Streaming potentials and permeability of saturated sandstones under triaxial stress. Consequence for electrotelluric anomalies prior to earthquakes, *J. Geophys. Res.*, *100*, 10,197–10,209.

Kulessa, B., B. Hubbard, and G. H. Brown (2003a), Cross-coupled flow modeling of coincident streaming and electrochemical potentials, and application to subglacial self-potential (SP) data, *J. Geophys. Res.*, *108*(B8), 2381, doi:10.1029/2001JB001167.

Kulessa, B., B. Hubbard, G. H. Brown, and J. Becker (2003b), Earth tide forcing of glacier drainage, *Geophys. Res. Lett.*, *30*(1), 1011, doi:10.1029/2002GL015303.

Leroy, P., and A. Revil (2004), A triple layer model of the surface electrochemical properties of clay minerals, *J. Colloid Interface Sci.*, *270*(2), 371–380.

Levenston, M. E., E. H. Frank, and A. J. Grodzinsky (1999), Electrokinetic and poroelastic coupling during finite deformations of charged porous media, *J. Appl. Mech.*, *66*, 323–333.

Li, Y., and D. W. Oldenburg (1998), 3-D inversion of gravity data, *Geophysics*, *63*(1), 109–119.

Linde, N., A. Revil, A. Bolève, C. Dagès, J. Castermant, B. Suski, and M. Voltz (2007), Estimation of the water table throughout a catchment using self-potential and piezometric data in a Bayesian framework, *J. Hydrol.*, *334*, 88–98.

Lippmann, M. J., and G. S. Bodvarsson (1983), Numerical studies of the heat and mass transport in the Cerro Prieto geothermal field, Mexico, *Water Resour. Res.*, *19*, 753–767.

Lippman, M. J., A. H. Truesdell, S. E. Halfman, and A. Mañon (1991), A review of the hydrogeological-geochemical model for Cerro Prieto, *Geothermics*, *20*, 39–52.

Loke, M. H., and R. D. Barker (1996), Rapid least-squares inversion of apparent resistivity pseudosections by a quasi-Newton method, *Geophys. Prospect.*, *44*, 131–152.

Lyons, D. J., and P. C. van de Kamp (1980), Subsurface geological and geophysical study of the Ceerro Prieto geothermal field, Report LBL-10540, Lawrence Berkeley Laboratory, Berkeley, Calif.

Manon, A., E. Mazor, M. Jimenez, A. Sanchez, J. Fausto, and C. Zennijo (1977), Extensive geochemical studies in the geothermal field of Cerro Prieto, Mexico, LBB report 7019, 113 pp.

Massenet, F., and V. N. Pham (1985), Experimental and theoretical basis of self-potential phenomena in volcanic areas with reference to results obtained on Mount Etna (Sicily), *Earth Planet. Sci. Lett.*, *73*, 415–429.

Menke, W. (1989), *Geophysical Data Analysis: Discrete Inverse Theory, International Geophysics Series*, vol. 45, 289 pp., Acad. Press, London.

Minsley, B. J., J. Sogade, and F. D. Morgan (2007a), Three-dimensional source inversion of self-potential data, *J. Geophys. Res.*, *112*, B02202, doi:10.1029/2006JB004262.

Minsley, B. J., J. Sogade, and F. D. Morgan (2007b), Three-dimensional self-potential inversion for subsurface DNAPL contaminant detection at the Savannah River Site, South Carolina, *Water Resour. Res.*, *43*, W04429, doi:10.1029/2005WR003996.

Moore, J. R., and S. D. Glaser (2007), Self-potential observations during hydraulic fracturing, *J. Geophys. Res.*, *112*, B02204, doi:10.1029/2006JB004373.

Naudet, V., A. Revil, J.-Y. Bottero, and P. Bégassat (2003), Relationship between self-potential (SP) signals and redox conditions in contaminated groundwater, *Geophys. Res. Lett.*, *30*(21), 2091, doi:10.1029/2003GL018096.

Naudet, V., A. Revil, E. Rizzo, J.-Y. Bottero, and P. Bégassat (2004), Groundwater redox conditions and conductivity in a contaminant plume from geoelectrical investigations, *Hydrol. Earth Syst. Sci.*, *8*(1), 8–22.

Overbeek, J. Th. G. (1952), Electrochemistry of the double layer, in *Colloid Science, 1, Irreversible Systems*, edited by H. R. Kruyt, pp. 115–193, Elsevier, New York.

Palciauskas, V. V., and P. A. Domenico (1989), Fluid pressures in deforming porous rocks, *Water Resour. Res.*, *25*, 203–213.

Park, S. K., W. Dalrymple, and J. C. Larsen (2007), The 2004 Parkfield earthquake: Test of the electromagnetic precursor hypothesis, *J. Geophys. Res.*, *112*, B05302, doi:10.1029/2005JB004196.

Parker, R. L. (1977), Understanding inverse theory, *Annu. Rev. Earth Planet. Sci.*, *5*, 35–64.

Pascal-Marquis, R. D., M. Esslen, K. Kochi, and D. Lehmann (2002), Functionnal imaging with low resolution brain electromagnetic tomography (LORETA): Review, new comparisons, and new validation, *Jpn. J. Clin. Neurophysiol.*, *30*, 81–94.

Patella, D. (1997), Self-potential global tomography including topographic effects, *Geophys. Prospect.*, *45*, 843–863.

Paul, K. (1965), Direct interpretation of self-potential anomalies caused by inclined sheets of infinite horizontal extensions, *Geophysics*, *30*, 418–423.

Pengra, D. B., S. X. Li, and P.-Z. Wong (1999), Determination of rock properties by low-frequency AC electrokinetics, *J. Geophys. Res.*, *104*, 29,485–29,508.

Perrier, F., M. Trique, B. Lorne, J.-P. Avouac, S. Hautot, and P. Tarits (1998), Electrical potential variations associated with yearly lake level variations, *Geophys. Res. Lett.*, *25*, 1955–1959.

Petiau, G. (2000), Second generation of lead-lead chloride electrodes for geophysical applications, *Pure Appl. Geophys.*, *157*, 357–382.

Polster, W., and H. L. Barnes (1994), Comparative hydrodynamic and thermal characteristics of sedimentary basins and geothermal systems in sediment-filled rift valleys, in *Basin Compartments and Seals*, edited by P. J. Ortoleva, 477 pp., AAPG Memoir, 61, 437–457, American Association of Petroleum Geologists, Tulsa, Okla.

Revil, A. (1995), Conductivité Electrique et Potentiel Spontané dans les Mileux Poreux: De la Théorie à l'Analyse des Mesures en Forage, Ph.D. thesis, Université Louis Pasteur, Strasbourg, France.

Revil, A. (1999), Ionic diffusivity, electrical conductivity, membrane and thermoelectric potentials in colloids and granular porous media: A unified model, *J. Colloid Interface Sci.*, *212*, 503–522.

Revil, A. (2002), Genesis of mud volcanoes in sedimentary basins. A solitary wave-based mechanism, *Geophys. Res. Lett.*, *29*(12), 1574, doi:10.1029/2001GL014465.

Revil, A. (2007), Thermodynamics of transport of ions and water in charged and deformable porous media, *J. Colloid Interface Sci.*, *307*(1), 254–264.

Revil, A., and L. M. Cathles (2002), Fluid transport by solitary waves along growing faults: A field example from the South Eugene Island Basin, Gulf of Mexico, *Earth Planet. Sci. Lett.*, *6313*, 1–15, (erratum, EPSL, 204, 321–322, 2002).

Revil, A., and P. Leroy (2001), Hydroelectric coupling in a clayey material, *Geophys. Res. Lett.*, *28*(8), 1643–1646.

Revil, A., and P. Leroy (2004), Constitutive equations for ionic transport in porous shales, *J. Geophys. Res.*, *109*, B03208, doi:10.1029/2003JB002755.

Revil, A., and N. Linde (2006), Chemico-electromechanical coupling in microporous media, *J. Colloid Interface Sci.*, *302*, 682–694.

Revil, A., and P. A. Pezard (1998), Streaming electrical potential anomaly along faults in geothermal areas, *Geophys. Res. Lett.*, *25*(16), 3197–3200.

Revil, A., P. A. Pezard, and P. W. J. Glover (1999a), Streaming potential in porous media: 1. Theory of the zeta-potential, *J. Geophys. Res.*, *104*(B9), 20,021–20,031.

Revil, A., H. Schwaeger, L. M. Cathles, and P. Manhardt (1999b), Streaming potential in porous media: 2. Theory and application to geothermal systems, *J. Geophys. Res.*, *104*(B9), 20,033–20,048.

Revil, A., L. Ehouarne, and E. Thyreault (2001), Tomography of self-potential anomalies of electrochemical nature, *Geophys. Res. Lett.*, *28*(23), 4363–4366.

Revil, A., D. Hermitte, M. Voltz, R. Moussa, J.-G. Lacas, G. Bourrié, and F. Trolard (2002), Self-potential signals associated with variations of the hydraulic head during an infiltration experiment, *Geophys. Res. Lett.*, *29*(7), 1106, doi:10.1029/2001GL014294.

Revil, A., G. Saracco, and P. Labazuy (2003a), The volcano-electric effect, *J. Geophys. Res.*, *108*(B5), 2251, doi:10.1029/2002JB001835.

Revil, A., V. Naudet, J. Nouzaret, and M. Pessel (2003b), Principles of electrography applied to self-potential electrokinetic sources and hydrogeological applications, *Water Resour. Res.*, *39*(5), 1114, doi:10.1029/2001WR000916.

Revil, A., P. Leroy, and K. Titov (2005a), Characterization of transport properties of argillaceous sediments. Application to the Callovo-Oxfordian Argillite, *J. Geophys. Res.*, *110*, B06202, doi:10.1029/2004JB003442.

Revil, A., L. Cary, Q. Fan, A. Finizola, and F. Trolard (2005b), Self-potential signals associated with preferential ground water flow pathways in a buried paleo-channel, *Geophys. Res. Lett.*, *32*, L07401, doi:10.1029/2004GL022124.

Revil, A., N. Linde, A. Cerepi, D. Jougnot, S. Matthäi, and S. Finsterle (2007), Electrokinetic coupling in unsaturated porous media, *J. Colloid Interface Sci.*, *313*(1), 315–327, doi:10.1016/j.jcis.2007.03.037.

Rizzo, E., B. Suski, A. Revil, S. Straface, and S. Troisi (2004), Self-potential signals associated with pumping-tests experiments, *J. Geophys. Res.*, *109*, B10203, doi:10.1029/2004JB003049.

Rodríguez, M. H., H. G. Puente, and J. de León V (2000), Update fluid flow model for the CP1 area of the Cerro Prieto geothermal field, Proceedings, 25th Workshop on Geothermal Reservoir Engineering, Stanford University, Stanford, California, January 24–26, 2000, SGP-TR-165, 10 pp.

Rozycki, A., J. M. R. Fonticiella, and A. Cuadra (2006), Detection and evaluation of horizontal fractures in Earth dams using self-potential method, *Eng. Geol.*, *82*(3), 145–153.

Sill, W. R. (1983), Self-potential modeling from primary flows, *Geophysics*, *48*, 76–86.

Soloviev, S. P., and J. J. Sweeney (2005), Generation of electric and magnetic field during detonation of high explosive charges in boreholes, *J. Geophys. Res.*, *110*, B01312, doi:10.1029/2004JB003223.

Spinelli, L. (1999), Analyse Spatiale de l'Activité Electrique Cérébrale: Nouveaux Développements, Ph.D. thesis (in French), 136 pp., Université Joseph Fourier-Grenoble I, Grenoble, France,

Storz, H., W. Storz, and F. Javobs (2000), Electrical resistivity tomography to investigate geological structures of the earth's upper crust, *Geophys. Prospect.*, *48*, 455–471.

Straface, S., C. Falico, S. Troisi, E. Rizzo, and A. Revil (2007), Estimating of the transmissivities of a real aquifer using self potential signals associated with a pumping test, *Ground Water*, *45*(4), 420–428.

Suski, B., A. Revil, K. Titov, P. Konosavsky, C. Dagès, M. Voltz, and O. Huttel (2006), Monitoring of an infiltration experiment using the self-potential method, *Water Resour. Res.*, *42*, W08418, doi:10.1029/2005WR004840.

Tikhonov, A. N., and V. Y. Arsenin (1977), *Solutions of Ill-posed Problems*, John Wiley, Washington, D. C.

Titov, K. V., A. Levitski, P. K. Konosavski, A. V. Tarasov, Y. T. Ilyin, and M. A. Buès (2005a), Combined application of surface geoelectrical methods for groundwater-flow modeling: A case history, *Geophysics*, *70*(5), H21–H31.

Titov, K., A. Revil, P. Konasovsky, S. Straface, and S. Troisi (2005b), Numerical modeling of self-potential signals associated with a pumping test experiment, *Geophys. J. Int.*, *162*, 641–650.

Trique, M., F. Perrier, T. Froidefond, J. P. Avouac, and S. Hautot (2002), Fluid flow near reservoir lakes inferred from the spatial and temporal analysis of the electric potential, *J. Geophys. Res.*, *107*(B10), 2239, doi:10.1029/2001JB000482.

Trujillo-Barreto, N. J., E. Aubert-Vásquez, and P. A. Valdès-Sosa (2004), Bayesian model averaging in EEG-MEG imaging, *NeuroImage*, *21*, 1300–1319.

Wilt, M. J., and N. E. Goldstein (1981), Resistivity monitoring at Cerro Prieto, *Geothermics*, *10*, 183–193.

Wishart, D. N., L. D. Slater, and A. E. Gates (2006), Self-potential improves characterization of hydraulically-active fractures from azimuthal geoelectrical measurements, *Geophys. Res. Lett.*, *33*, L17314, doi:10.1029/2006GL027092.

Yoshida, S. (2001), Convection current generated prior to rupture in saturated rocks, *J. Geophys. Res.*, *106*(B2), 2103–2120.

Yoshida, S., and T. Ogawa (2004), Electromagnetic emissions from dry and wet granite associated with acoustic emissions, *J. Geophys. Res.*, *109*, B09204, doi:10.1029/2004JB003092.

Yungul, S. H. (1950), Interpretation of spontaneous polarization anomalies caused by spheroidal ore bodies, *Geophysics*, *15*, 237–246.

Zablocki, C. J. (1976), Mapping thermal anomalies on an active volcano by the self-potential method, Kilauea, Hawaii, in *Proc. 2nd U. N. Symp. on the Development and Use of Geothermal Resources*, *2*, San Francisco, CA, v2, pp. 1299–1309, US Govt. Printing Office, Washington DC.

A. Bolève, Sobesol-Fugro, Savoie Technolac, BP 230, F-73375 Le Bourget-du-Lac CEDEX, France.

J. P. Dupont, CNRS-University of Rouen, UMR 6143 Morphodynamique Continentale et Côtière, 76821, Mont Saint Aignan, France.

A. Jardani and A. Revil, Department of Geophysics, Colorado School of Mines, 1500 Illinois Street, Golden, CO 80401, USA. (arevil@mines.edu)